Multi-band Carrier Phase Positioning toward 6G: Performance Bounds and Efficient Estimators

Citation for the original published paper (version of record):

Shourezari, E., Kaltiokallio, O., Ilter, M. et al (2026). Multi-band Carrier Phase Positioning toward 6G: Performance Bounds and Efficient Estimators. IEEE Transactions on Wireless Communications, 25: 18153-18170. http://dx.doi.org/10.1109/TWC.2026.3694524

Multi-Band Carrier Phase Positioning Toward 6G: Performance Bounds and Efficient Estimators

Ehsan Shourezari, *Graduate Student Member, IEEE*, Ossi Kaltiokallio, *Member, IEEE*,
Mehmet C. Ilter, *Senior Member, IEEE*, Jukka Talvitie, *Member, IEEE*,
Gonzalo Seco-Granados, *Fellow, IEEE*, Henk Wymeersch, *Fellow, IEEE*, and Mikko Valkama, *Fellow, IEEE*

***Abstract*—In addition to satellite systems, carrier phase positioning (CPP) is gaining attraction also in terrestrial mobile networks, particularly in 5G New Radio (NR) evolution toward 6G. One key challenge is to resolve the so-called integer ambiguity problem, as the carrier phase provides only relative position information. This work introduces and studies a multi-band CPP scenario with intra- and inter-band carrier aggregation (CA) opportunities across FR1, mmWave-FR2, and emerging 6G FR3 bands. Specifically, we derive multi-band CPP performance bounds, showcasing the superiority of multi-band CPP for high-precision localization in current and future mobile networks, while noting also practical imperfections such as clock offsets between the user equipment (UE) and the network as well as mutual clock imperfections between the network nodes. A wide collection of numerical results is provided, covering the impacts of the available carrier bandwidth, number of aggregated carriers, transmit power, and the number of network nodes or base stations. The offered results highlight that only two carriers suffice to substantially facilitate resolving the integer ambiguity problem while also largely enhancing the robustness of positioning against imperfections imposed by the network-side clocks and multi-path propagation. In addition, we also propose a two-stage practical estimator framework that achieves the derived bounds under all realistic bandwidth and transmit power conditions. Furthermore, we show that with an additional search-based refinement step, the proposed estimator becomes particularly suitable for narrowband Internet of Things (IoT) applications operating efficiently even under narrow carrier bandwidths. Finally, both the derived bounds and the proposed estimators are extended to scenarios where the bands assigned to each base station are nonuniform or fully disjoint, enhancing the practical deployment flexibility.**

***Index Terms*—5G NR and 6G, carrier aggregation, carrier phase positioning, Cramér-Rao bound, efficient estimators, integer ambiguity resolution, mixed-integer CRB, narrowband positioning.**

Received 10 October 2025; revised 28 February 2026 and 8 May 2026; accepted 15 May 2026. Date of publication 27 May 2026; date of current version 5 June 2026. This work was supported in part by the Business Finland under the 6G-ISAC Project and by the Research Council of Finland under Grant 352754, Grant 359095, and Grant 367800; in part by the Spanish Agency of Research (AEI) under Grant PID2023–152820OB–I00 funded by MICIU/AEI/10.13039/501100011033, in part by ERDF/EU; in part by the Generalitat de Catalunya AGAUR–ICREA Academia Program; in part by the SNS JU Project 6G-DISAC under the EU's Horizon Europe Research and Innovation Program under Grant 101139130, and in part by the Swedish Research Council (VR) through under Project 2022-03007. An earlier version of this paper was presented at IEEE ICC 2026 [32]. The associate editor coordinating the review of this article and approving it for publication was E. Leitinger. *(Corresponding author: Mikko Valkama.)*

Ehsan Shourezari, Ossi Kaltiokallio, Mehmet C. Ilter, Jukka Talvitie, and Mikko Valkama are with Tampere University, 33100 Tampere, Finland (e-mail: mikko.valkama@tuni.fi).

Gonzalo Seco-Granados is with the Universitat Autònoma de Barcelona, 08193 Bellaterra, Spain.

Henk Wymeersch is with the Chalmers University of Technology, 412 96 Gothenburg, Sweden.

Digital Object Identifier 10.1109/TWC.2026.3694524

I. Introduction

THE 3$^{\text{rd}}$ Generation Partnership Project (3GPP) Release 17 and 18 standards are setting stringent positioning requirements, targeting centimeter-level accuracy [1], which makes centimeter-level positioning a key feature in next-generation terrestrial mobile communication systems. *Carrier phase positioning (CPP)* is known to enable precise ranging, facilitating accuracies from sub-meter down to centimeter levels [2]. CPP methods are already well-established in the global navigation satellite system (GNSS) context, via either precise point positioning (PPP) or real-time kinematic (RTK) methods [3], while the use of carrier phase measurements has recently been explored also in 3GPP standardization, particularly in the context of 5G-Advanced, as an emerging technology for enhanced positioning capabilities [4]. Unlike other range-based positioning methods and the related delay measurements, whose accuracy depends on the signal bandwidth [5], [6], carrier phase measurements are independent of the signal bandwidth, whether obtained using a phase locked loop (PLL) [7], [8] or classical estimators [9].

A. Fundamentals and Prior Art

In general, the core principle of CPP lies in accurately measuring the carrier phase, enabling ranging precision within fractions of a wavelength [2]. A key technical challenge in utilizing carrier phase measurements is the *integer ambiguity problem* [10] which results from the fact that the carrier phase does not reveal the integer number of full wavelengths between the transmitter and the receiver. Furthermore, in most systems, achieving strict time synchronization between the nodes is challenging, and clock biases can impede accurate integer ambiguity estimation in single-point positioning [11]. The integer ambiguity problem can be addressed by combining phase and time measurements using conventional integer least-squares (ILS) solvers, or by performing double-differential phase measurements across multiple base station (BS) pairs and applying recursive filters, such as the Kalman filter, to tighten the integer search space [12]. More recently, [13] proposed a deep learning–based classification approach to estimate the integer ambiguities from phase-only measurements. On the other hand, synchronization can be directly addressed through inter-BS pilot transmission and clock bias estimation methods, which enable highly accurate synchronization on the order of picoseconds [14], [15].

In the context of 5G New Radio (NR) mobile networks, the CPP has been recently studied in [9], [15], [16], [17], and [18], with main focus on single-band measurements and signal processing algorithms. In [9], the authors introduced and derived performance bounds for localizing a user equipment (UE) under a common clock bias using time-of-arrival (ToA) and phase measurements, while in [16] and [17], carrier phase-based positioning and ranging has been investigated in indoor and Industrial Internet-of-Things (IIoT) scenarios. Furthermore, beyond static scenarios, [15], [18] have considered multi-snapshot CPP in dynamic scenarios. Specifically, [15] solves the CPP problem using a batch of multi-snapshot measurements, whereas [18] employs a real-time extended Kalman filtering approach for this purpose. Both works take into account the common challenge of tracking the integer ambiguity, commonly referred to as a cycle slip, which occurs when an abrupt change in the measured carrier phase arises due to loss of lock in the PLL. By detecting and re-estimating the integer ambiguities, the cycle-slip problem can be effectively mitigated.

In parallel, carrier aggregation (CA) is a key technology in modern mobile networks, enabling the aggregation of fragmented spectrum resources [19] for increased data rates. The NR CA mechanism applies to FR1 (sub-6 GHz) and FR2 (24.25–71 GHz), supporting various band combinations. Additionally, new spectrum allocations are expected for 6G networks within the 7–24 GHz range (FR3), which balances wider bandwidth, lower attenuation, and reduced hardware costs [20]. Importantly, CA can improve also the achievable positioning accuracy as it enlarges the effective bandwidth by combining positioning reference signals (PRS) from multiple component carriers [21]. To this end, [22] proposed joint estimation of ToA using reference symbols obtained from multiple frequency bands, while [23] demonstrated that a multi-band mechanism can create a virtual large frequency aperture, enabling improved multi-path resolution, which is a major challenge in recovering the line-of-sight (LoS) channel features for positioning. Similarly, [24] proposed a CA-based integrated sensing and communication mechanism for improved sensing performance.

Furthermore, in GNSS context, multi-band CPP is commonly harnessed through dual- and triple-band measurements. For the global positioning system (GPS), these typically employ the civilian bands L1, L2, and L5, enabling more effective ionospheric error correction and improved positioning accuracy [25], [26], [27], [28]. Finally, recent studies on multiple-frequency CPP in cellular networks, such as [29], have exploited carrier aggregation to mitigate cycle-slip challenges in joint position and orientation tracking problems, while [30] and [31] exploit the carrier phases of closely spaced OFDM subcarriers within a single band, where combined phase measurements are used to facilitate integer ambiguity resolution. However, since this approach is effective for subcarriers that are very close in frequency, it cannot be readily extended to CA-based true multi-band scenarios. And very importantly, the existing CPP studies do not present sufficiently tight performance benchmarks or fundamental bounds reflecting the true potential of multi-band CPP, while also lack practical estimation algorithms able to reach the realistic tight bounds.

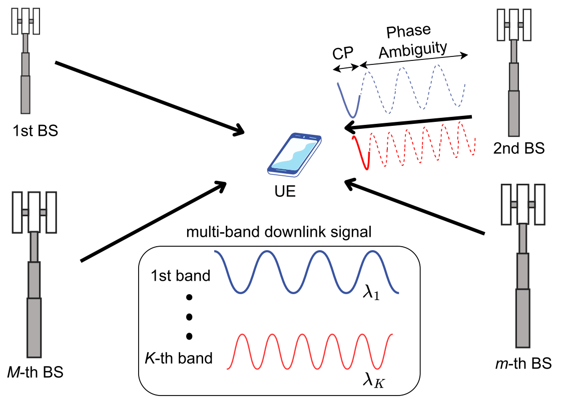

Fig. 1. Illustration of the multi-band CPP system model with K bands and M network nodes.

B. Novelty and Contributions

In this article, building on our initial work in [32], we investigate the multi-band CPP problem illustrated conceptually in Fig. 1. We focus on the single-snapshot setting, which also serves as a fundamental building block for multi-snapshot routines such as Kalman filtering or batch estimation. Moreover, when the user kinematic model is highly uncertain, single-snapshot positioning becomes particularly relevant. Therefore, understanding the fundamental performance of snapshot localization is essential, even within multi-snapshot processing frameworks. Specifically, while targeting to fill the above-noted gaps in the existing literature, we derive the fundamental performance bounds for both intra- and inter-band CA scenarios across all three frequency ranges (FR1, FR2, and FR3) in terms of the *mixed-integer Cramér-Rao bound (MICRB)*. We develop and formulate the related multi-band observation models, while also design and propose practical efficient estimators shown to be able to reach the derived bounds, and analyze their feasibility and performance under different system configurations. The key technical contributions and scientific novelty of this work can be stated as follows:

- We formulate a single-snapshot model for the delay and phase observations in multi-band multiple-BS downlink transmission context, explicitly highlighting the integer ambiguity problem. Based on this model, we introduce and derive the MICRB, specifically tailored for the considered multi-band observation model. This provides the fundamental position error bound (PEB) for cellular multi-band CPP;
- We propose a multi-band CPP estimation algorithm that is efficient in performance and achieves the derived bounds under all realistic configurations in terms of transmit power and carrier bandwidth. Unlike the methods in [30] and [31], the proposed algorithm is not restricted to specific frequencies or subcarriers and operates effectively for any aggregation of bands. In addition, we develop two search-based variants of the algorithm that preserve estimator efficiency even in low-bandwidth deployments and applications such as the Internet of Things (IoT);

- We address the robustness of the proposed CPP methods against practical imperfections, covering mutual clock impairments between the network nodes as well as multipath propagation. We show that the multi-band operation allows for largely increased robustness against the considered practical impairments.
- We investigate the feasibility of CPP and the proposed algorithms across different scenarios, where each BS operates on a potentially different subset of bands, while also highlight the importance of calibrated phase offsets among the bands through this analysis.

Overall, we utilize the derived bounds and the numerical results to gain and offer valuable insights into how multi-band operation affects the feasibility of integer ambiguities resolution and the effective use of carrier phase measurements for future cellular positioning.

The rest of this article is organized as follows. Section II presents the system model. In Section III, we introduce the multi-band observation model tailored for the CPP problem and integer programming, derive the fundamental multi-band bounds, and extend them to scenarios with network-side synchronization impairments. Section IV proposes a two-stage CPP estimator along with its search-based variants, concluding with a computational complexity analysis. In Section V, the proposed estimator is extended to the case of nonuniform BS-band assignment. Section VI presents and analyzes the numerical results, where the bounds and estimator performance are examined under various parameter settings, and the tightness of the bounds is verified. Sensitivity and robustness analyses against network-side clock impairments and multipath propagation are also provided. Conclusions are drawn in Section VII, while selected mathematical details are given in the Appendixes.

Notations: Italic letters x denote scalars, while lowercase $\boldsymbol{x}$ and uppercase $\boldsymbol{X}$ in boldface represent vectors and matrices, respectively. The superscript $()^\top$ denotes the transpose operation. The operator $\|\cdot\|$ denotes the Euclidean norm, $|\cdot|$ denotes either the absolute value of a number or the cardinality of a set, and $\lfloor x \rfloor$ denotes the greatest integer less than or equal to x. The operator $\otimes$ denotes the Kronecker product, $\mathrm{diag}\,(\boldsymbol{x})$ outputs a diagonal matrix with the elements of a vector $\boldsymbol{x}$ on the diagonals, $\mathrm{blkdiag}(\cdot,\cdot)$ does the same thing for multiple matrix inputs and generates a block diagonal matrix, $\nabla_{\boldsymbol{x}}(\cdot)$ is the Jacobian matrix of its operand wrt. $\boldsymbol{x}$, and $\mathrm{tr}(\boldsymbol{X})$ refers to the trace of $\boldsymbol{X}$.

II. MULTI-BAND CPP SYSTEM MODEL

We consider a scenario with a single UE and $M \geq N_d + 1$ BSs, where $N_d \in \{2,3\}$ represents the dimension of the position coordinates (i.e., 2D or 3D positions, respectively). The UE has an unknown position $\boldsymbol{x}_{\mathrm{ue}} \in \mathbb{R}^{N_d}$ and is subject to clock bias wrt. the BSs. We further assume that the BSs are mutually time- and phase-synchronized and have known locations $\boldsymbol{x}_{\mathrm{bs},m} \in \mathbb{R}^{N_d}$ [9]. The impact of BS-BS synchronization imperfections is separately covered later in Section III-D. Terminology-wise, we note that we use the notion of 'BS', however, the system model is also applicable with distributed transmission/reception points (TRPs) of a single BS–or similarly with TRPs or antenna points of a future cell-free system.

At the k-th band, each BS transmits a unit-modulus OFDM reference signal for M OFDM symbols, e.g., 5G PRS, over N_k subcarriers with subcarrier spacing $\Delta_{f,k}$ and transmit power $P_{\mathrm{tx},k}$. The reference signal transmission of the M BSs are orthogonalized, with each BS utilizing different subcarriers per OFDM symbol following the classical comb structure. At the UE side, the frequency-domain received signal from m-th BS and k-th band under the ideal LoS[1] reads [33]

$$\boldsymbol{y}_{m,k} = \sqrt{E_{s,k}}\alpha_{m,k}\boldsymbol{d}(\tau_{m,k}) + \boldsymbol{\omega}_{m,k}, \tag{1}$$

such that $\boldsymbol{y}_{m,k} \in \mathbb{C}^{N_k \times 1}$. Herein, $E_{s,k} = P_{\mathrm{tx},k}/(N_k \Delta_{f,k})$ is the energy per subcarrier, $\alpha_{m,k} = \rho_{m,k} e^{-j2\pi\vartheta_{m,k}}$ represents the complex channel gain in which $\rho_{m,k}$ captures the effect of path loss and transmitter and receiver antenna gains, $\vartheta_{m,k}$ is the normalized carrier phase (expressed in cycles), $\tau_{m,k}$ is the ToA (delay), and $\boldsymbol{d}(\tau_{m,k})$ is the channel response of the m-th BS for the k-th band with $[\boldsymbol{d}(\tau_{m,k})]_n = e^{-j2\pi n \Delta_{f,k}\tau_{m,k}}$ for $n \in \{0,\cdots,N_k-1\} - (N_k-1)/2$, and $k \in \{1,\ldots,K\}$. The additive white Gaussian noise (AWGN) $\boldsymbol{\omega}_{m,k} \in \mathbb{C}^{N_k \times 1}$ has the statistics $\boldsymbol{\omega}_{m,k} \sim \mathcal{N}(\boldsymbol{0}, \sigma_\omega^2 \boldsymbol{I})$, where σ_ω^2 stands for the noise power spectral density.[2] Moreover, the noise vectors for different bands or BSs are assumed to be mutually independent.

Since the BSs are mutually synchronized, the actual ToA and carrier phase values across multiple frequency bands and BSs characterize the geometric relationship between the UE and the BSs. This can be expressed as [34]

$$\tau_{m,k} = \frac{1}{c}\|\boldsymbol{x}_{\mathrm{bs},m} - \boldsymbol{x}_{\mathrm{ue}}\| + B_{\mathrm{ue}} \tag{2}$$

$$\vartheta_{m,k} = \frac{1}{\lambda_k}\|\boldsymbol{x}_{\mathrm{bs},m} - \boldsymbol{x}_{\mathrm{ue}}\| + f_{c,k}B_{\mathrm{ue}} + \varphi_{\mathrm{ue},k} \tag{3}$$

where $\tau_{m,k}$ is the actual ToA in the time domain, and $\vartheta_{m,k}$ is the actual carrier phase in cycles. Here, B_{ue} is the clock bias of the UE relative to the network/BSs clock that is propagated to both the delay and carrier phase measurements, $\varphi_{\mathrm{ue,k}}$ is the UE phase offset (in cycles), assumed to be band-dependent for generality, and $f_{c,k} = c/\lambda_k$ is the carrier frequency of the k-th band. Furthermore, c denotes the speed-of-light and λ_k is the wavelength corresponding to $f_{c,k}$.

The considered multi-band CPP approach follows a two-stage estimation process. First, after the preliminary time and frequency synchronization stages, the ToA and carrier phase are estimated from $\boldsymbol{y}_{m,k}$, expressed conceptually as $\hat{\tau}_{m,k}$ and $\hat{\vartheta}_{m,k}$. Then, these estimates are used to determine the UE position. Note that $\hat{\vartheta}_{m,k}$ is an estimate of the fractional part of $\vartheta_{m,k}$. Hence, we can express the ToA and phase measurements as effective distances $y_{\tau,m,k} = \hat{\tau}_{m,k} \times c$ and $y_{\vartheta,m,k} = \hat{\vartheta}_{m,k}\lambda_k$, given by

$$y_{\tau,m,k} = \|\boldsymbol{x}_{\mathrm{bs},m} - \boldsymbol{x}_{\mathrm{ue}}\| + B_{\mathrm{ue}}c + \omega_{\tau,m,k} \tag{4}$$

---

[1] Impact of non-line-of-sight propagation paths is explicitly considered along the numerical results section, as part of the robustness analyses.

[2] This is an assumption made for simplicity, but everything can be easily generalized for the case where σ_ω^2 depends on k.

$$\begin{aligned} y_{\vartheta,m,k} = {} & \|\boldsymbol{x}_{\mathrm{bs},m} - \boldsymbol{x}_{\mathrm{ue}}\| + B_{\mathrm{ue}}c + z_{m,k}\lambda_k \\ & + \varphi_{\mathrm{ue},k}\lambda_k + \omega_{\vartheta,m,k}. \end{aligned} \tag{5}$$

Herein, $z_{m,k} \in \mathbb{Z}$ is the *unknown integer ambiguity*, with the actual value given by

$$z_{m,k} = -\left\lfloor \vartheta_{m,k} + \frac{\omega_{\vartheta,m,k}}{\lambda_k} \right\rceil. \tag{6}$$

The terms $\omega_{\tau,m,k}$ and $\omega_{\vartheta,m,k}$ represent zero-mean Gaussian noise affecting the ToA and phase measurements or observations, respectively. Both terms are expressed in the distance domain, and are independent of each other. By deriving the Fisher information matrix (FIM) for the physical signal model in (1) wrt. $\tau_{m,k}$ and $\vartheta_{m,k}$, and applying a selected numerical approximation similar to [9], it can be shown that the lower bounds for the covariance of $\omega_{\tau,m,k}$ and $\omega_{\vartheta,m,k}$ are equal to

$$\sigma^2_{\tau,m,k} = 3c^2/(2\,\gamma_{m,k}\pi^2 W_k^2), \tag{7}$$

$$\sigma^2_{\vartheta,m,k} = \lambda_k^2/(8\,\gamma_{m,k}\pi^2), \tag{8}$$

respectively. Herein, $\gamma_{m,k}$ is the signal-to-noise-energy ratio–referred to as SNR in the continuation. This can be expressed as

$$\gamma_{m,k} = N_k E_{s,k}\rho^2_{m,k}/\sigma^2_\omega \tag{9}$$

where $W_k = N_k\Delta_{f,k}$ denotes the available passband width (available bandwidth) at band k.

Finally, by gathering the observations from different BSs and frequency bands, we define $\boldsymbol{y} = \left[\boldsymbol{y}_\tau^\top, \boldsymbol{y}_\vartheta^\top\right]^\top$ where both $\boldsymbol{y}_\tau$ and $\boldsymbol{y}_\vartheta$ are structured as $\boldsymbol{y}_\star = \left[y_{\star,1,1}, y_{\star,2,1}, \ldots, y_{\star,M,K}\right]^\top \in \mathbb{R}^{KM\times 1}$. Similarly, we build the effective noise vectors $\boldsymbol{\omega}_\tau$, $\boldsymbol{\omega}_\vartheta \in \mathbb{R}^{\mathrm{KM}\times 1}$ by gathering $\omega_{\tau,m,k}$ and $\omega_{\vartheta,m,k}$, respectively. Their corresponding diagonal covariance matrices are defined as $\boldsymbol{\Sigma}_\tau = \operatorname{diag}\left([\sigma^2_{\tau,1,1}, \sigma^2_{\tau,2,1}, \ldots, \sigma^2_{\tau,M,K}]^\top\right)$, and $\boldsymbol{\Sigma}_\vartheta = \operatorname{diag}\left([\sigma^2_{\vartheta,1,1}, \sigma^2_{\vartheta,2,1}, \ldots, \sigma^2_{\vartheta,M,K}]^\top\right)$, respectively. We further introduce $\boldsymbol{\eta} = \left[\boldsymbol{s}^\top, \boldsymbol{z}^\top\right]^\top \in \mathbb{R}^{(K+N_d+1)\times 1} \times \mathbb{Z}^{KM\times 1}$ as the *unknown parameter vector*, where $\boldsymbol{z} = \left[z_{1,1}, z_{2,1}, \ldots, z_{M,K}\right]^\top$ and $\boldsymbol{s} = \left[\boldsymbol{x}_{\mathrm{ue}}^\top, B_{\mathrm{ue}}, \boldsymbol{\varphi}_{\mathrm{ue}}^\top\right]^\top \in \mathbb{R}^{(K+N_d+1)\times 1}$, while $\boldsymbol{\varphi}_{\mathrm{ue}} = \left[\varphi_{\mathrm{ue},1}, \ldots, \varphi_{\mathrm{ue},K}\right]^\top$.

III. MULTI-BAND CPP PERFORMANCE BOUNDS

In this section, we introduce and derive a novel performance bound for the multi-band CPP problem that explicitly accounts for the mixed-integer nature of the observations–thus referred to as the MICRB. Alongside the MICRB, we establish a multi-band delay-only bound, which is derived using more ordinary FIM formulations. This bound provides useful insights and serves as a benchmark for comparison purposes. Furthermore, the bounds are also extended to account for practical synchronization impairments between the BSs, allowing for further insight and design requirements for future distributed networks.

A. Multi-Band Observation Model

We first organize and express the stacked delay and phase observations in (4)-(5) as

$$\boldsymbol{y} = \tilde{\boldsymbol{f}}(\tilde{\boldsymbol{s}}) + \boldsymbol{B}\boldsymbol{z} + \boldsymbol{B}\boldsymbol{\varphi} + \boldsymbol{\omega}, \tag{10}$$

where $\tilde{\boldsymbol{s}} = \left[\boldsymbol{x}_{\mathrm{ue}}^\top, B_{\mathrm{ue}}\right]^\top$, $\boldsymbol{\varphi} = \boldsymbol{\varphi}_{\mathrm{ue}} \otimes \mathbf{1}_{M\times 1} \in \mathbb{R}^{KM\times 1}$. The matrix $\boldsymbol{B}$ is defined as $\boldsymbol{B} = \left[\mathbf{0}_{KM\times KM}\,\boldsymbol{\Lambda}\right]^\top$ with $\boldsymbol{\Lambda} = \operatorname{diag}([\lambda_1, \cdots, \lambda_K]^\top) \otimes \boldsymbol{I}_M \in \mathbb{R}^{KM\times KM}$. The noise is stacked as $\boldsymbol{\omega} = \left[\boldsymbol{\omega}_\tau^\top, \boldsymbol{\omega}_\vartheta^\top\right]^\top$ with $\boldsymbol{\omega} \sim \mathcal{N}(\mathbf{0}_{2KM\times 1}, \boldsymbol{\Sigma}_{\mathrm{ch}})$, and $\boldsymbol{\Sigma}_{\mathrm{ch}} = \operatorname{blkdiag}(\boldsymbol{\Sigma}_\tau, \boldsymbol{\Sigma}_\vartheta)$, while $\tilde{\boldsymbol{f}}(\cdot)$ is a nonlinear function of $\tilde{\boldsymbol{s}}$, defined for $j = 1, 2, \cdots, 2KM$ as

$$[\tilde{\boldsymbol{f}}(\tilde{\boldsymbol{s}})]_j = \|\boldsymbol{x}_{\mathrm{bs},\mathrm{mod}(j-1,M)+1} - \boldsymbol{x}_{\mathrm{ue}}\| + B_{\mathrm{ue}}c. \tag{11}$$

We next note that $\boldsymbol{\varphi}$ and $\boldsymbol{z}$ are not jointly identifiable, and the system of equations is under-determined. To address this, since both $\boldsymbol{z}$ and $\boldsymbol{\varphi}_{\mathrm{ue}}$ are eventually nuisance parameters, the state dimension can be reduced by incorporating $\varphi_{\mathrm{ue},k}$ into one of the integer ambiguities of the corresponding band. Without loss of generality, if we merge each $\varphi_{\mathrm{ue},k}$ with $z_{1,k}$, the reduced-state variables for the k-th band become $\varphi_{\mathrm{d},k} = \varphi_{\mathrm{ue},k} + z_{1,k}$ and $[z_{2,k} - z_{1,k}, \ldots, z_{M,k} - z_{1,k}]^\top \in \mathbb{Z}^{(M-1)\times 1}$, instead of the original $\varphi_{\mathrm{ue},k}$ and $[z_{1,k}, \ldots, z_{M,k}]^\top \in \mathbb{Z}^{M\times 1}$. Accordingly, the observation model can be reformulated using the combined parameters as

$$\boldsymbol{y} = \tilde{\boldsymbol{f}}(\tilde{\boldsymbol{s}}) + \boldsymbol{B}\boldsymbol{E}\boldsymbol{z}_{\mathrm{d}} + \boldsymbol{B}\boldsymbol{\varphi}_{\mathrm{d}} + \boldsymbol{\omega}, \tag{12}$$

where $\boldsymbol{z}_{\mathrm{d}} = \boldsymbol{D}\boldsymbol{z} \in \mathbb{Z}^{K(M-1)\times 1}$ denotes the multi-band differential (reduced-dimension) integer ambiguity vector, and the combined phase offset vector is $\boldsymbol{\varphi}_{\mathrm{d}} = \boldsymbol{\varphi}_{\mathrm{d,ue}} \otimes \mathbf{1}_{M\times 1} \in \mathbb{R}^{KM\times 1}$ with $\boldsymbol{\varphi}_{\mathrm{d,ue}} = [\varphi_{\mathrm{d},1}, \cdots, \varphi_{\mathrm{d},K}]^\top$. Both $\boldsymbol{D}$ and $\boldsymbol{E}$ are block-diagonal matrices, with each block corresponding to a band. Matrix $\boldsymbol{D} = \boldsymbol{I}_K \otimes \left[-\mathbf{1}_{(M-1)\times 1}\;\boldsymbol{I}_{(M-1)}\right] \in \mathbb{R}^{K(M-1)\times KM}$ acts as a differentiator, reducing the integer parameters dimension in each band. Furthermore, matrix $\boldsymbol{E} = \boldsymbol{I}_K \otimes \left[\mathbf{0}_{(M-1)\times 1}\;\boldsymbol{I}_{(M-1)}\right]^\top \in \mathbb{R}^{KM\times K(M-1)}$ inserts a zero element as the first row of each reduced-dimension integer block.

Now, we can collect all the real-valued unknowns into $\boldsymbol{f}(\boldsymbol{s}) = \tilde{\boldsymbol{f}}(\tilde{\boldsymbol{s}}) + \boldsymbol{B}\boldsymbol{\varphi}_{\mathrm{d}}$ and rewrite (12) as

$$\boldsymbol{y} = \boldsymbol{f}(\boldsymbol{s}) + \boldsymbol{B}\boldsymbol{E}\boldsymbol{z}_{\mathrm{d}} + \boldsymbol{\omega}. \tag{13}$$

This observation model serves as the basis of the MICRB derivation, in which with a slight change of variables, $\boldsymbol{s}$ is redefined as $\boldsymbol{s} = \left[\boldsymbol{x}_{\mathrm{ue}}^\top, B_{\mathrm{ue}}, \boldsymbol{\varphi}_{\mathrm{d,ue}}^\top\right]^\top \in \mathbb{R}^{(K+N_d+1)\times 1}$.

B. Multi-Band Known-Integer and Mixed-Integer CRBs

1) Methodology: For conventional estimation problems with ordinary real- or complex-valued parameters, such as ToA-based positioning, the lower bound on the error covariance of any unbiased estimator is obtained from the diagonal elements of the inverse of the FIM [35]. This is known as the Cramér-Rao Bound (CRB), while an unbiased estimator whose covariance matrix equals the CRB is called an efficient estimator. In general, the FIM quantifies how sharply the likelihood function varies around the true parameter values—essentially, how much curvature the likelihood function exhibits. If the log-likelihood function of the observation vector $\boldsymbol{o}$ wrt. the parameter vector $\boldsymbol{\theta}$ is denoted as $L(\boldsymbol{o};\boldsymbol{\theta})$, the FIM is given by $\mathrm{FIM} = \mathbb{E}[\nabla_{\boldsymbol{\theta}} L(\boldsymbol{o};\boldsymbol{\theta})\,(\nabla_{\boldsymbol{\theta}} L(\boldsymbol{o};\boldsymbol{\theta}))^\top]\big|_{\boldsymbol{\theta}_{\mathrm{true}}}$ [35].

However, in the CPP problem at hand, the conventional FIM approach cannot be applied since the above derivatives cannot be computed with respect to *integer-valued* parameters. Instead, we derive and compute the so-called multi-band mixed-integer CRB as follows: We first assume that the relaxed integer ambiguities, considered as ordinary real numbers, are given with the error covariance equal to the CRB of the relaxed observation model. Next, to incorporate the integer nature of the parameters into the bound derivation, we find the ILS estimation of the ambiguities. This transforms the remaining part of the problem into the *real-valued* domain, referred to as the *known-integer* problem. However, any error in the estimated integer ambiguities from the ILS stage introduces a bias in $\boldsymbol{s}$. Thus, in the final stage, we compute the MICRB as the lower bound for the error covariance of a biased estimator of $\boldsymbol{s}$, based on the theoretical framework presented in [36].

2) Established Bounds: As stated, we start by assuming that the real-valued relaxed ambiguity variables are given, with an error covariance equal to the corresponding CRB. Before proceeding, we ensure that all parameters are identifiable in the relaxed observation model. Using (12) as the baseline, the observation model with the relaxed identifiable parameters takes the form

$$\boldsymbol{y} = \tilde{\boldsymbol{f}}(\tilde{\boldsymbol{s}}) + \boldsymbol{B}\boldsymbol{z}_{\text{rlx}} + \boldsymbol{\omega}. \tag{14}$$

Through this, by computing the CRB of $\boldsymbol{z}_{\text{rlx}} \in \mathbb{R}^{KM\times 1}$, denoted by $\boldsymbol{\Sigma}_{\text{rlx}}$, we can express the given real-valued ambiguities as follows

$$\hat{\boldsymbol{z}}_{\text{rlx}} = \boldsymbol{E}\boldsymbol{z}_{\text{d}} + \boldsymbol{\varphi}_{\text{d}} + \boldsymbol{u}, \quad \boldsymbol{u} \sim \mathcal{N}(\boldsymbol{0}_{KM\times 1}, \boldsymbol{\Sigma}_{\text{rlx}}). \tag{15}$$

The detailed expression of $\boldsymbol{\Sigma}_{\text{rlx}}$ is provided in Appendix A. Next, to eliminate the term $\boldsymbol{\varphi}_{\text{d}}$ in $\hat{\boldsymbol{z}}_{\text{rlx}}$, we multiply both sides of (15) by $\boldsymbol{D}$ and obtain the differential observation

$$\boldsymbol{r} = \boldsymbol{D}\boldsymbol{E}\boldsymbol{z}_{\text{d}} + \boldsymbol{D}\boldsymbol{\varphi}_{\text{d}} + \boldsymbol{D}\boldsymbol{u} = \boldsymbol{z}_{\text{d}} + \boldsymbol{D}\boldsymbol{u}, \tag{16}$$

which follow from the equalities of $\boldsymbol{D}\boldsymbol{E} = \boldsymbol{I}$ and $\boldsymbol{D}\boldsymbol{\varphi}_{\text{d}} = \boldsymbol{0}$. To prove the first equality, note that both $\boldsymbol{D}$ and $\boldsymbol{E}$ are block-diagonal matrices, so their product is also block-diagonal, with each block satisfying $\left[-\boldsymbol{1}_{(M-1)\times 1}\ \boldsymbol{I}_{(M-1)}\right] \times \left[\boldsymbol{0}_{(M-1)\times 1}\ \boldsymbol{I}_{(M-1)}\right]^{\top} = \boldsymbol{I}_{(M-1)}$. For the second equality, we know $\boldsymbol{\varphi}_{\text{d}}$ consists of K subvectors, the k-th one being $\varphi_{\text{d},k} \times \boldsymbol{1}_{M\times 1}$. The block multiplication with $\boldsymbol{D}$ cancels the constant entries in each subvector, resulting in the zero vector. Finally, we recover $\boldsymbol{z}_{\text{d}}$ by solving the ILS problem, written as

$$\hat{\boldsymbol{z}}_{\text{d}} = \underset{\boldsymbol{z}_{\text{d}} \in \mathbb{Z}^{K(M-1)\times 1}}{\arg\min}\ (\boldsymbol{r} - \boldsymbol{z}_{\text{d}})^{\top}\boldsymbol{S}^{-1}(\boldsymbol{r} - \boldsymbol{z}_{\text{d}}), \tag{17}$$

where $\boldsymbol{S} = \boldsymbol{D}\boldsymbol{\Sigma}_{\text{rlx}}\boldsymbol{D}$.

In general, any error in $\boldsymbol{z}_{\text{d}}$ leads to a bias in $\boldsymbol{s}$. To determine this bias, we linearize (13) around $\boldsymbol{s}$, which yields $\boldsymbol{y} = \boldsymbol{f}(\boldsymbol{s}) + \boldsymbol{A}_{\boldsymbol{f}}(\boldsymbol{s})\boldsymbol{\delta s} + \boldsymbol{B}\boldsymbol{E}\boldsymbol{z}_{\text{d}} + \boldsymbol{\omega}$, where $\boldsymbol{A}_{\boldsymbol{f}}(\boldsymbol{s}) = \nabla_{\boldsymbol{s}}\boldsymbol{f}(\boldsymbol{s}) \in \mathbb{R}^{2KM\times(K+N_d+1)}$ is computed at the true value of $\boldsymbol{s}$. The explicit form of $\boldsymbol{A}_{\boldsymbol{f}}(\boldsymbol{s})$ is provided in the next section, in Eq. (28). In the absence of any error in $\boldsymbol{z}_{\text{d}}$, i.e., when $\hat{\boldsymbol{z}}_{\text{d}} = \boldsymbol{z}_{\text{d}}$, the WLS estimate of $\boldsymbol{\delta s}$ is given by

$$\widehat{\boldsymbol{\delta s}} = \left(\boldsymbol{\Sigma}_{\text{ch}}^{-1/2}\boldsymbol{A}_{\boldsymbol{f}}(\boldsymbol{s})\right)^{\dagger}\boldsymbol{\Sigma}_{\text{ch}}^{-1/2}\left(\boldsymbol{y} - \boldsymbol{f}(\boldsymbol{s}) - \boldsymbol{B}\boldsymbol{E}\hat{\boldsymbol{z}}_{\text{d}}\right), \tag{18}$$

which is an unbiased[3] zero-mean estimator. However, if there is an integer error $\boldsymbol{\delta}_z$ in the solution to the integer problem (17), such that $\hat{\boldsymbol{z}}_{\text{d}} = \boldsymbol{z}_{\text{d}} + \boldsymbol{\delta}_z$, the resulting estimate $\widehat{\boldsymbol{\delta s}}$ will have a bias given by

$$\boldsymbol{b}(\boldsymbol{s}|\boldsymbol{\delta}_z) = -\left(\boldsymbol{\Sigma}_{\text{ch}}^{-1/2}\boldsymbol{A}_{\boldsymbol{f}}(\boldsymbol{s})\right)^{\dagger}\boldsymbol{\Sigma}_{\text{ch}}^{-1/2}\boldsymbol{B}\boldsymbol{E}\boldsymbol{\delta}_z \tag{19}$$

Now, the observation model is turned into a known integer one, meaning that there is no longer any integer unknown in the problem. In order to compute the MICRB, we first note that when the estimators of $\boldsymbol{s}$ are biased with bias $\boldsymbol{b}(\boldsymbol{s}|\boldsymbol{\delta}_z)$, the corresponding lower bound of the error covariance, accounting for such bias, is given by [36]

$$\begin{aligned}\boldsymbol{\Sigma}_{\text{mi}}(\boldsymbol{s}|\boldsymbol{\delta}_z) &= \boldsymbol{b}(\boldsymbol{s}|\boldsymbol{\delta}_z)\boldsymbol{b}(\boldsymbol{s}|\boldsymbol{\delta}_z)^{\top}\\ &\quad + \Big(\boldsymbol{I} + \boldsymbol{A}_{\boldsymbol{b}}(\boldsymbol{s})\Big)\boldsymbol{\Sigma}_{\text{known}}(\boldsymbol{s})\Big(\boldsymbol{I} + \boldsymbol{A}_{\boldsymbol{b}}(\boldsymbol{s})\Big)^{\top}\end{aligned} \tag{20}$$

where $\boldsymbol{A}_{\boldsymbol{b}}(\boldsymbol{s}) = \nabla_{\boldsymbol{s}}\boldsymbol{b}(\boldsymbol{s}|\boldsymbol{\delta}_z) \in \mathbb{R}^{(K+N_d+1)\times(K+N_d+1)}$. In the usual case that the bias is not very sensitive to small variations of $\boldsymbol{s}$, we can approximate that $\boldsymbol{A}_b(\boldsymbol{s}) \approx \boldsymbol{0}$, and $\boldsymbol{\Sigma}_{\text{known}}(\boldsymbol{s})$ represents the *ultimate lower bound* on the error covariance matrix for the measurement model in which the reduced-state integer ambiguity vector, $\boldsymbol{z}_{\text{d}}$, is assumed to be known. The detailed formulation of the matrix $\boldsymbol{J}_{\text{known}}(\boldsymbol{s}) = \boldsymbol{\Sigma}_{\text{known}}^{-1}(\boldsymbol{s})$ can be found in Appendix B. The corresponding bound is called *known-integer bound* in the following.

Finally, the proposed MICRB on the error covariance can be obtained by taking the expectation with respect to the integer ambiguity error. This is expressed as

$$\boldsymbol{\Sigma}_{\text{mi}}(\boldsymbol{s}) = \mathbb{E}_{\boldsymbol{\delta}_z}\Big[\boldsymbol{\Sigma}_{\text{mi}}(\boldsymbol{s}|\boldsymbol{\delta}_z)\Big] \approx \frac{1}{N_{\text{mc}}}\sum_{i=1}^{N_{\text{mc}}}\boldsymbol{\Sigma}_{\text{mi}}(\boldsymbol{s}|\boldsymbol{\delta}_z^{(i)}), \tag{21}$$

where N_{mc} is the number of Monte-Carlo simulations, serving as the basis for numerical computations. Since (17) is invariant wrt. $\boldsymbol{z}_{\text{d}}$, the Monte-Carlo approach simplifies to generating N_{mc} samples of a Gaussian noise, $\boldsymbol{r}^{(i)} \sim \mathcal{N}(\boldsymbol{0}_{K(M-1)\times 1}, \boldsymbol{S})$, and directly determining the integer error $\boldsymbol{\delta}_z^{(i)} = \hat{\boldsymbol{z}}_{\text{d}}^{(i)}$ using (17). Hence, the floating solution of the original problem is actually not needed to obtain the MICRB. Eventually, by considering the clock bias and phase offsets as unknown nuisance parameters, the marginal MICRB for the user position will be obtained from $\boldsymbol{\Sigma}_{\text{mi}}(\boldsymbol{x}_{\text{ue}}) = [\boldsymbol{\Sigma}_{\text{mi}}(\boldsymbol{s})]_{1:N_d,1:N_d}$. Thus, computing the MICRB requires only the geometry matrix $\boldsymbol{A}_{\boldsymbol{f}}(\boldsymbol{s})$, along with $\boldsymbol{\Sigma}_{\text{rlx}}$, $\boldsymbol{\Sigma}_{\text{ch}}$, $\boldsymbol{\Sigma}_{\text{known}}$. An overall holistic block diagram illustrating the proposed MICRB is depicted in Fig. 2.

C. Multi-Band Delay-Only Reference Bound

As an important reference or benchmark, besides the known-integer bound, we consider the bound for the observation model that exploits only the ToA measurements and thus drops $\boldsymbol{y}_{\vartheta}$. In this case, the unknown parameters will

---

[3] Strictly speaking, the unbiasedness holds under the linearized model. Because $\boldsymbol{f}$ is nonlinear, the estimator is approximately unbiased, but the approximation is highly accurate except when noise dominates.

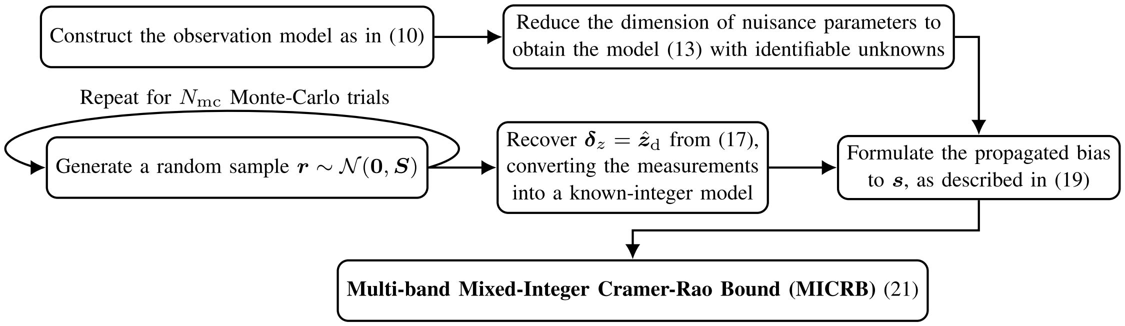

Fig. 2. Block diagram illustration of deriving and computing the multi-band mixed-integer Cramér-Rao bound.

be $\tilde{\boldsymbol{s}} = \left[\boldsymbol{x}_{\mathrm{ue}}^\top, B_{\mathrm{ue}}\right]^\top$, and the corresponding FIM can be formulated as

$$\boldsymbol{J}_{\mathrm{delay}}(\tilde{\boldsymbol{s}}) = \begin{bmatrix} \tilde{\boldsymbol{U}} \boldsymbol{J}_\tau \tilde{\boldsymbol{U}}^\top & c\,\tilde{\boldsymbol{U}}\operatorname{diag}(\boldsymbol{J}_\tau) \\ c(\tilde{\boldsymbol{U}}\operatorname{diag}(\boldsymbol{J}_\tau))^\top & \operatorname{tr}(\boldsymbol{J}_\tau)c^2 \end{bmatrix}, \tag{22}$$

where $\boldsymbol{J}_\tau = \boldsymbol{\Sigma}_\tau^{-1}$, and $\tilde{\boldsymbol{U}} = \mathbf{1}_{1\times K} \otimes \boldsymbol{U} \in \mathbb{R}^{N_d \times KM}$ denotes the transposed Jacobian matrix of $[\tilde{\boldsymbol{f}}(\tilde{\boldsymbol{s}})]_{1:KM}$ wrt. $\boldsymbol{x}_{\mathrm{ue}}$, with $\boldsymbol{U} = [\boldsymbol{u}_1, \boldsymbol{u}_2, \ldots, \boldsymbol{u}_M]$, and $\boldsymbol{u}_{\mathrm{m}} = (\boldsymbol{x}_{\mathrm{ue}} - \boldsymbol{x}_{\mathrm{bs},m})/\|\boldsymbol{x}_{\mathrm{ue}} - \boldsymbol{x}_{\mathrm{bs},m}\|$.[4] Then, we obtain $\boldsymbol{\Sigma}_{\mathrm{delay}}(\boldsymbol{x}_{\mathrm{ue}}) = \left[\boldsymbol{J}_{\mathrm{delay}}^{-1}(\tilde{\boldsymbol{s}})\right]_{1:N_d,1:N_d}$. This lower bound is greater in value than the known-integer bound since it completely disregards the phase measurements. Thus, the difference between the delay-only bound and the derived known-integer and mixed-integer bounds tells the potential performance gains available through the phase measurements.

D. Extension to System With Network/BS Clock Imperfections

While the above derivations assume perfect mutual synchronization among the BSs, achieving such in practice is challenging, and each BS may exhibit an individual residual clock bias relative to a reference BSs. While most existing works [16], [37] address this issue by employing an additional reference receiver and applying double-differential measurements, in our scenario these imperfections cannot be estimated from the available measurements nor eliminated through differential methods. Thus, to characterize their impact, we instead model the imperfections as random variables with given statistics.

To this end, we next extend the previous bounds to an imperfectly synchronized network by modeling BS-dependent clock imperfections as additional random terms, $\tilde{B}_m \sim \mathcal{N}(0, \delta_m^2)$ [15], added to both the ToA and carrier phase observation models in (4) and (5). The modified observations become

$$y_{\tau,m,k} = \|\boldsymbol{x}_{\mathrm{bs},m} - \boldsymbol{x}_{\mathrm{ue}}\| + B_{\mathrm{ue}}c + \tilde{B}_m c + \omega_{\tau,m,k} \tag{23}$$

$$\begin{aligned} y_{\vartheta,m,k} = {} & \|\boldsymbol{x}_{\mathrm{bs},m} - \boldsymbol{x}_{\mathrm{ue}}\| + z_{m,k}\lambda_k + \varphi_{\mathrm{ue},k}\lambda_k \\ & + B_{\mathrm{ue}}c + \tilde{B}_m c + \omega_{\vartheta,m,k}. \end{aligned} \tag{24}$$

Now, the new random terms can be treated as additional noise components and incorporated into the error covariance matrices $\boldsymbol{\Sigma}_\tau$, and $\boldsymbol{\Sigma}_\vartheta$. Specifically, we augment both the diagonal entries and the entries corresponding to correlated measurements with a term $\delta_m^2 c^2$. The updated noise covariance matrices are then given by $\tilde{\boldsymbol{\Sigma}}_\tau = \boldsymbol{\Sigma}_\tau + \boldsymbol{\Sigma}_{\mathrm{im}}$ and $\tilde{\boldsymbol{\Sigma}}_\vartheta = \boldsymbol{\Sigma}_\vartheta + \boldsymbol{\Sigma}_{\mathrm{im}}$ where

$$\boldsymbol{\Sigma}_{\mathrm{im}} = c^2 \mathbf{1}_{K\times K} \otimes \operatorname{diag}\left([\delta_1^2, \ldots, \delta_M^2]^\top\right). \tag{25}$$

This formulation captures the full correlation of the imperfections across the bands while assuming independence across different BSs. To also account for full correlation between ToA and carrier phase measurements, the composite covariance matrix is re-expressed as

$$\tilde{\boldsymbol{\Sigma}}_{\mathrm{ch}} = \boldsymbol{\Sigma}_{\mathrm{ch}} + \mathbf{1}_{2\times 2} \otimes \boldsymbol{\Sigma}_{\mathrm{im}}. \tag{26}$$

IV. PROPOSED MULTI-BAND CPP ESTIMATORS

To determine the UE position with a practical estimation procedure, we divide the CPP problem into two stages. First, we obtain an *initial estimate* of the UE coordinates via the delay measurements following the closed-form estimation approach in [38] extended to multi-band measurements. Then, in the second stage, we consider both the delay and phase observations to establish the *final estimate*. Given the initial coordinate estimate from the first stage, we linearize the observation model around it. We then compute the relaxed integer ambiguities using a weighted least squares (WLS) approach and subsequently resolve them in the integer domain using ILS techniques. With both the initial coordinate estimate and integer ambiguities determined, the UE position estimate is refined accordingly.

A. First Stage: TDoA-Based Initial Estimation

For the ToA measurements in (4), there are well-known localization methods based on time difference of arrival (TDoA) combinations [38], [39], [40], [41], as well as gradient-based techniques such as Gauss-Newton or gradient descent. Among these, the algorithm proposed by Amiri et al. [38], inspired by the spherical intersection method [42], offers several advantages. First, it provides a closed-form solution, which ensures low computational complexity and avoids the need for hyperparameter tuning. Second, as noted in [38], the estimator is statistically efficient and achieves performance very close to the corresponding CRB–a behavior that we also observe in our simulations. Finally, the algorithm requires only

---

[4] All $\tilde{\boldsymbol{U}}$, $\boldsymbol{U}$, and $\boldsymbol{u}_m$ depend on $\boldsymbol{x}_{\mathrm{ue}}$, but the argument $(\boldsymbol{x}_{\mathrm{ue}})$ is omitted for notational simplicity.

a modest number of measurements, i.e., a minimum of four in a three-dimensional setting.

While the original formulation in [38] addresses or considers a classical single-band case, we extend it to the multi-band scenario. To this end, we use the measurement corresponding to the band–BS pair with the minimum delay error variance as the reference[5] and then construct the $KM-1$ TDoA measurements. The remainder of the algorithm remains unchanged. For further details, the reader is referred to [38] for presentation brevity.

B. Second Stage: Applying Carrier Phase Measurements

In the second stage, we refine the initial estimate–denoted by $\hat{\boldsymbol{x}}_{\mathrm{ue},0}$–by incorporating also the carrier phase measurements. Since the observation model is nonlinear with respect to the UE position and cannot be solved analytically, we linearize it around $\hat{\boldsymbol{x}}_{\mathrm{ue},0}$ using a first-order Taylor expansion. The parameters B_{ue} and $\varphi_{\mathrm{d,ue}}$ appear linearly in (13), and thus their initial values can be set arbitrarily; for simplicity, they are initialized to zero. Accordingly, we define the initial estimate of the unknown vector $\boldsymbol{s}$ as $\boldsymbol{s}_0 = [\hat{\boldsymbol{x}}_{\mathrm{ue},0}, \mathbf{0}_{1\times(K+1)}]^\top$, and the Taylor expansion of the observation model around $\boldsymbol{s}_0$ yields

$$\boldsymbol{y} \simeq \boldsymbol{f}(\boldsymbol{s}_0) + \boldsymbol{A}_{\boldsymbol{f}}(\boldsymbol{s}_0)\boldsymbol{\delta s} + \boldsymbol{B}\boldsymbol{E}\boldsymbol{z}_{\mathrm{d}} + \boldsymbol{\omega}, \tag{27}$$

where $\boldsymbol{A}_{\boldsymbol{f}}(\boldsymbol{s}_0) = \nabla_{\boldsymbol{s}}\boldsymbol{f}(\boldsymbol{s})\big|_{\boldsymbol{s}_0} \in \mathbb{R}^{2KM\times(K+N_d+1)}$ is the Jacobian matrix evaluated at $\boldsymbol{s}_0$. This can be expressed as

$$\boldsymbol{A}_{\boldsymbol{f}}(\boldsymbol{s}_0) = \begin{bmatrix} \tilde{\boldsymbol{U}}^\top & c\times\mathbf{1}_{KM\times 1} & \mathbf{0}_{KM\times K} \\ \tilde{\boldsymbol{U}}^\top & c\times\mathbf{1}_{KM\times 1} & \tilde{\mathbf{\Lambda}}^\top \end{bmatrix}, \tag{28}$$

where $\tilde{\mathbf{\Lambda}} = \mathrm{diag}([\lambda_1,\cdots,\lambda_K]^\top)\otimes\mathbf{1}_{1\times\mathrm{M}} \in \mathbb{R}^{\mathrm{K}\times\mathrm{KM}}$, and $\tilde{\boldsymbol{U}}^\top$ is now calculated at the estimated coordinates $\hat{\boldsymbol{x}}_{\mathrm{ue},0}$.

Next, by moving all known terms to the left-hand side of (27) and grouping the unknown variables into a single vector, we obtain the compact linear form

$$\tilde{\boldsymbol{y}} \simeq \begin{bmatrix} \boldsymbol{A}_{\boldsymbol{f}}(\boldsymbol{s}_0) & \boldsymbol{B}\boldsymbol{E} \end{bmatrix} \begin{bmatrix} \boldsymbol{\delta s} \\ \boldsymbol{z}_{\mathrm{d}} \end{bmatrix} + \boldsymbol{\omega}, \tag{29}$$

where $\tilde{\boldsymbol{y}} = \boldsymbol{y} - \boldsymbol{f}(\boldsymbol{s}_0)$. We now apply the WLS method to obtain the relaxed estimate $\hat{\boldsymbol{z}}_{\mathrm{d,rlx}} \in \mathbb{R}^{K(M-1)\times 1}$ of $\boldsymbol{z}_{\mathrm{d}}$. To recover the integer estimate of $\boldsymbol{z}_{\mathrm{d}}$, we follow the same procedure outlined in problem (17), where the matrix $\boldsymbol{S}$ is replaced here with the error covariance of the estimation method, denoted by $\widehat{\boldsymbol{S}}$. Here, $\widehat{\boldsymbol{S}}$ represents the error covariance matrix associated with the WLS estimate of $\boldsymbol{z}_{\mathrm{d}}$ from the observation model (29), and it corresponds to the lower-right $K(M-1)\times K(M-1)$ block of the full WLS covariance matrix $\widehat{\boldsymbol{C}}$, given by[6]

$$\widehat{\boldsymbol{C}} = \left[\left(\left[\boldsymbol{A}_{\boldsymbol{f}}(\boldsymbol{s}_0)\ \boldsymbol{B}\boldsymbol{E}\right]^\top \mathbf{\Sigma}_{\mathrm{ch}}^{-1} \left[\boldsymbol{A}_{\boldsymbol{f}}(\boldsymbol{s}_0)\ \boldsymbol{B}\boldsymbol{E}\right]\right)^{-1}\right]. \tag{30}$$

It is worth noting that any well-known integer programming method, such as the Least-squares AMBiguity Decorrelation Adjustment (LAMBDA) approach [43], can be employed to solve the related integer problem. Once the integer estimate $\hat{\boldsymbol{z}}_{\mathrm{d}}$ is obtained, we return to (29), move the known terms to the left-hand side, and solve for the remaining unknown, which is the update term $\boldsymbol{\delta s}$. The final WLS problem then reads as

$$\tilde{\tilde{\boldsymbol{y}}} \simeq \boldsymbol{A}_{\boldsymbol{f}}(\boldsymbol{s}_0)\boldsymbol{\delta s} + \boldsymbol{\omega}, \tag{31}$$

where $\tilde{\tilde{\boldsymbol{y}}} = \tilde{\boldsymbol{y}} - \boldsymbol{B}\boldsymbol{E}\hat{\boldsymbol{z}}_{\mathrm{d}}$. After estimating $\widehat{\boldsymbol{\delta s}}$, the solution is updated as $\hat{\boldsymbol{s}} = \boldsymbol{s}_0 + \widehat{\boldsymbol{\delta s}}$.

To further improve the estimation accuracy, the second stage of the algorithm can be repeated iteratively. At the end of each iteration, the updated solution $\hat{\boldsymbol{s}}$ is used as the new linearization point $\boldsymbol{s}_0$ for the next iteration. The final estimate is taken as the value of $\hat{\boldsymbol{s}}$ obtained in the last iteration. As demonstrated in the numerical results, only two iterations of the second stage are typically sufficient to achieve high estimation accuracy, although a more general exit or stopping criterion can also be considered. Overall, as demonstrated through the numerical results in Section V, the algorithm converges efficiently to the mixed-integer bound under a broad range of system parameters, and can thus be called an efficient estimator.

C. Search-Based Refinements of the First Stage Solution

Since the maximum likelihood (ML) cost function of the observation model in (13) is non-convex and may contain numerous local minima, obtaining a sufficiently accurate solution in the first stage of the algorithm is crucial. However, the accuracy achievable in the first stage is fundamentally limited by the delay-only PEB. Therefore, as we will observe through the numerical results, under narrowband configurations, even efficient delay-only estimators may fail to provide an adequately accurate initial solution for the CPP problem.

To address this challenge, we propose to estimate the delay-only FIM at the obtained initial solution, $\boldsymbol{s}_0$, and use the corresponding error covariance matrix, $\mathbf{\Sigma}_{\mathrm{delay}}(\boldsymbol{s}_0)$, to define a search region around $\boldsymbol{s}_0$. Within this region, a set of candidate points is generated, either randomly or deterministically, using

$$\hat{\boldsymbol{x}}_{\mathrm{ue},0}^{(n)} = \hat{\boldsymbol{x}}_{\mathrm{ue},0} + \boldsymbol{L}\boldsymbol{\xi}^{(n)} \tag{32}$$

such that the n-th candidate point can be defined as $\boldsymbol{s}_0^{(n)} = [\hat{\boldsymbol{x}}_{\mathrm{ue},0}^{(n)}, \mathbf{0}_{1\times(K+1)}]^\top$. In the above, $\mathbf{\Sigma}_{\mathrm{delay}}(\boldsymbol{s}_0) = \boldsymbol{L}\boldsymbol{L}^\top$ and $\boldsymbol{\xi}^{(n)}$ depends on the sampling method as follows:

- *Random Sampling*– Sampling is performed according to $\hat{\boldsymbol{x}}_{\mathrm{ue},0}^{(n)} \sim \mathcal{N}(\hat{\boldsymbol{x}}_{\mathrm{ue},0}, \mathbf{\Sigma}_{\mathrm{delay}}(\boldsymbol{s}_0))$, which can be achieved using (32) where $\boldsymbol{\xi}^{(n)}$ are independent standard normal variables, that is, $\boldsymbol{\xi}^{(n)} \sim \mathcal{N}(\mathbf{0}, \mathbf{1})$.
- *Deterministic Sampling*– The candidate points are generated using (32) in which $\boldsymbol{\xi}^{(n)}$ are formed as a Cartesian product of one-dimensional Gauss–Hermite quadratures [44]. The disadvantage of the method is that the p-th order Gauss–Hermite method generates p^2 candidate points, most of which are located in areas with extremely low probability when p is large. To save computational resources, the proposed deterministic sampling

---

[5] In practice, this corresponds to selecting the measurement with the largest effective bandwidth–SNR product.

[6] Alternatively, one can also use $\widehat{\boldsymbol{S}} = \boldsymbol{D}\hat{\mathbf{\Sigma}}_{\mathrm{rlx}}\boldsymbol{D}$, where $\hat{\mathbf{\Sigma}}_{\mathrm{rlx}}$ is computed at $\hat{\boldsymbol{x}}_{\mathrm{ue},0}$. However, the covariance matrix derived from (30) is preferred as it represents the actual error covariance of $\hat{\boldsymbol{z}}_{\mathrm{d,rlx}}$.

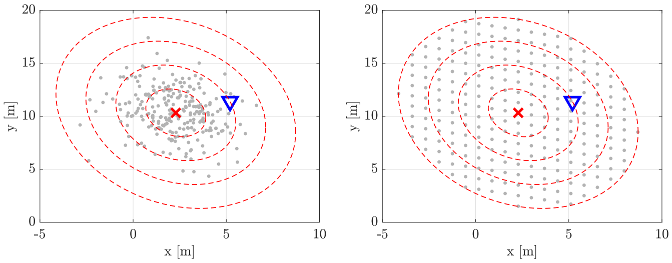

(a) Random Sampling (b) Deterministic Sampling

Fig. 3. Illustrative example of the considered sampling methods. In the figures, the true UE location is shown using a blue upside down triangle, $\hat{\boldsymbol{x}}_{\mathrm{ue},0}$ illustrated with a red cross, the $1\sigma - 4\sigma$ error ellipses shown with dashed red lines, and the generated samples visualized with gray markers. In the example, $N_s = 253$ for both methods and $T_\alpha = 4$ for deterministic sampling.

method thus only considers evaluation points that satisfy $\|\boldsymbol{\xi}^{(n)}\| \leq T_\alpha$ in which T_α is a user defined parameter.

An illustrative example of the proposed sampling methods is provided in Fig. 3.

The second-stage procedure is then applied to each of the candidate points, $\boldsymbol{s}_0^{(n)}$, and the one yielding the lowest ML cost (considering both delay and phase measurements) is selected. Now, let $\mathcal{C}_{\boldsymbol{s}}$ with $|\mathcal{C}_{\boldsymbol{s}}| = N_s$ denote the set of all initial candidate points. The final solution is obtained by solving the following discrete optimization problem of the form

$$n^\star = \underset{n \in \{1,\cdots,N_s\}}{\arg\min} \left(\boldsymbol{y} - \boldsymbol{f}(\hat{\boldsymbol{s}}^{(n)}) - \boldsymbol{B}\boldsymbol{E}\hat{\boldsymbol{z}}_{\mathrm{d}}^{(n)}\right)^\top \boldsymbol{\Sigma}_{\mathrm{ch}}^{-1} \times \left(\boldsymbol{y} - \boldsymbol{f}(\hat{\boldsymbol{s}}^{(n)}) - \boldsymbol{B}\boldsymbol{E}\hat{\boldsymbol{z}}_{\mathrm{d}}^{(n)}\right) \tag{33}$$

where $\hat{\boldsymbol{s}}^{(n)}$ and $\hat{\boldsymbol{z}}_{\mathrm{d}}^{(n)}$ are the estimated parameters when the n-th initialization point is used for the second stage. The final estimate is $\boldsymbol{s}^\star = \boldsymbol{s}^{(n^\star)}$ with $n^\star$ obtained from (33). Increasing the number of candidate points enhances the likelihood of approaching the MICRB, as more points are likely to fall within the attraction region of the final optimal solution. However, this comes at the cost of higher computational complexity.

The overall proposed approach is summarized in Algorithm 1.

D. Complexity Analysis

The first stage of the algorithm, which finds the TDoA solution in closed-form based on the multi-band extension of [38], has a computational complexity on the order of $\mathcal{O}((KM-1)^3)$. In the second stage, solving the real-domain WLS problems has a complexity of $\mathcal{O}(K_d^3 + KMK_d^2 + K^2M^2K_d)$, where $K_d = K + N_d + 1$. For the integer ambiguity resolution, the LAMBDA method has an overall complexity of $\mathcal{O}((K(M-1))^3 + \kappa^{K(M-1)})$, where $1 < \kappa \leq 2$. The first term corresponds to the decorrelation (reduction) stage, and the second term corresponds to the search stage [43]. However, as shown in [45], the Modified LAMBDA (MLAMBDA) method significantly improves efficiency in both stages by optimizing the search parameter κ. Finally, note that in the second stage, the overall complexity scales linearly with the number of search points, N_s, and number of iterations, N_{iter}.

Algorithm 1 Proposed Two-Stage TDoA-CPP Algorithm

```
Choose $N_{\mathrm{iter}} \geq 1$, $N_{\mathrm{s}}$, $T_\alpha$, and set $t = 1$.
Estimate the initial solution $\boldsymbol{s}_0$ based on the ToA observations in (4), using the multi-band extension of the algorithm in [38].
Find $\boldsymbol{\Sigma}_{\mathrm{delay}}(\boldsymbol{s}_0)$ based on (22).
Pick $N_{\mathrm{s}}$ random or deterministic points from the area defined by $\boldsymbol{\Sigma}_{\mathrm{delay}}(\boldsymbol{s}_0)$ (and $T_\alpha$ for the deterministic approach) around $\boldsymbol{s}_0$ and build the set $\mathcal{C}_{\boldsymbol{s}}$.
for each $\boldsymbol{s} \in \mathcal{C}_{\boldsymbol{s}}$ do
    Set $\boldsymbol{s}_0 \leftarrow \boldsymbol{s}$.
    repeat
        Linearize the full set of observations around $\boldsymbol{s}_0$ to obtain the model in (29).
        Estimate the relaxed real-valued solution $\hat{\boldsymbol{z}}_{\mathrm{d,rlx}}$ by applying WLS to (29).
        Estimate the integer ambiguities $\hat{\boldsymbol{z}}_{\mathrm{d}}$ by solving the ILS problem in (17), using the error covariance $\widehat{\boldsymbol{S}}$ from (30).
        Substitute $\hat{\boldsymbol{z}}_{\mathrm{d}}$ into (29) to obtain the model in (31), then estimate $\widehat{\boldsymbol{\delta s}}$.
        Update the solution: $\hat{\boldsymbol{s}} = \boldsymbol{s}_0 + \widehat{\boldsymbol{\delta s}}$.
        Set $\boldsymbol{s}_0 \leftarrow \hat{\boldsymbol{s}}$.
        Increment $t \leftarrow t + 1$.
    until $t > N_{\mathrm{iter}}$
    Buffer $\hat{\boldsymbol{s}}$, $\hat{\boldsymbol{z}}_{\mathrm{d}}$.
end for
Solve the problem (33) to obtain $\boldsymbol{s}^\star$ and $\boldsymbol{x}_{\mathrm{ue}}^\star$.
```

Overall, it is fair to conclude that there is notable computing complexity involved. However, in the cellular context, the main positioning task can be handled by a local server like the location management function (LMF) in the core network, with the UE providing only phase and delay measurements [2], [46]. This computational offloading, however, implies additional communication overhead. Therefore, developing reduced-complexity yet statistically efficient estimators is a way to alleviate the complexity–communication tradeoff and becomes an important topic for future research. To this end, several approaches can be considered, such as adaptive sampling strategies that adjust the number of candidate points based on the accuracy of the initial estimate. In addition, the multi-band structure can be exploited for complexity reduction by combining phase measurements across bands to form a virtual low-frequency phase observation, which can facilitate integer ambiguity resolution [47].

V. NONUNIFORM BS-BAND ASSIGNMENT

So far, we have assumed that all BSs communicate using the same set of frequency bands. In this section, for improved deployment flexibility, we generalize the proposed algorithm to scenarios with nonuniform BS-band assignments, where different BSs may transmit at different subsets of bands. We also consider an extreme case in which BSs operate at completely disjoints sets of bands, thereby highlighting the importance of providing a band-independent phase offset.

To this end, to extend the proposed algorithm to nonuniform BS-band assignments, we simply rearrange the observation model in (10) by stacking and grouping the observations corresponding to each band. In scenarios with band-dependent phase offsets ($\varphi_{\mathrm{ue},k}$), at least two phase measurements per band (i.e., two BSs have to transmit on the same band) are required to make the data exploitable for the CPP; otherwise, the terms $z_{m,k}$ and $\varphi_{\mathrm{ue},k}$ become indistinguishable. In contrast, when the phase offset is band-independent, the algorithm can be generalized to completely disjoint BS-band assignments. In the following subsections, we first address the case of nonuniform BS-band assignment under band-dependent phase offsets, and then consider the case of band-independent phase offsets.

A. Band-Dependent Phase Offsets

As noted above, for each band, we group the measurements and rearrange the observations. The first stage of the algorithm remains the same, applying TDoA-based localization to the new set of observations. In the second stage, the matrices used in the observation model (27) must be updated accordingly. To this end, we first construct the matrices $\boldsymbol{A}_{\boldsymbol{f}}(\boldsymbol{s}_0)$ and $\boldsymbol{B}$ assuming a full assignment of each BS to all existing bands (i.e., all KM possible combinations). We then remove the rows and columns corresponding to non-existing assignments. To construct $\boldsymbol{z}_{\mathrm{d}}$, we designate the first BS assigned to each specific band as the reference BS for that band and define the differential integer ambiguities accordingly. Based on this, we can derive and express the updated matrix $\boldsymbol{E}$. The same modification applies when deriving the performance bounds. The exact mathematical description is omitted for presentation brevity.

B. Band-Independent Phase Offsets

A band-independent phase offset is feasible and observed in practice when the responses of the transmitter and receiver chains (i.e., amplifiers, mixers, digital-to-analog/analog-to-digital converters, etc.) at the different bands are calibrated, that is to say, measured before using the system and compensated digitally during the subsequent system operation [23]. We note that in any case, a single shared oscillator has to be used in the transmitter and also in the receiver, since this is a prerequisite for having a band-independent clock bias, B_{ue}–an assumption that has been made throughout the article and work.

The band-independent phase offset scenario enables the CPP framework to handle a wider range of BS-band assignment types, including fully disjoint assignments, which are particularly useful under bandwidth resource constraints. We thus next first formulate the band-independent phase offset case for the fully uniform BS-band assignment, and then apply the same update procedure from the previous subsection to extend it to nonuniform assignments and completely disjoint sets of bands. Before proceeding, we note that, for the band-independent phase offset case, we use φ_{ue} instead of $\varphi_{\mathrm{ue},k}$, and the new set of real-valued unknowns becomes $\bar{\boldsymbol{s}} = \left[\boldsymbol{x}_{\mathrm{ue}}^{\top}, B_{\mathrm{ue}}, \varphi_{\mathrm{d}}\right]^{\top} \in \mathbb{R}^{(N_d+2)\times 1}$. In the fully uniform assignment case, $\varphi_{\mathrm{d}} = \varphi_{\mathrm{ue}} + z_{1,1}$ when choosing the first unknown integer ambiguity as the reference, again without lost of generality.

Since the delay measurements are intact, the first stage of the algorithm remains the same. However, due to the new definition of $\bar{\boldsymbol{s}}$, the linearized observation (27) now reads

$$\boldsymbol{y} \simeq \bar{\boldsymbol{f}}(\bar{\boldsymbol{s}}_0) + \overline{\boldsymbol{A}}_{\boldsymbol{f}}(\bar{\boldsymbol{s}}_0)\overline{\boldsymbol{\delta s}} + \boldsymbol{B}\overline{\boldsymbol{E}}\bar{\boldsymbol{z}}_{\mathrm{d}} + \boldsymbol{\omega}. \tag{34}$$

Here, $\bar{\boldsymbol{f}}(\bar{\boldsymbol{s}}) = \tilde{\boldsymbol{f}}(\tilde{\boldsymbol{s}}) + \mathrm{diag}(\boldsymbol{B})\varphi_{\mathrm{d}}$, and the Jacobian matrix evaluated at $\bar{\boldsymbol{s}}_0$ is $\overline{\boldsymbol{A}}_{\boldsymbol{f}}(\bar{\boldsymbol{s}}_0) = \nabla_{\bar{\boldsymbol{s}}}\bar{\boldsymbol{f}}(\bar{\boldsymbol{s}})\big|_{\bar{\boldsymbol{s}}_0} \in \mathbb{R}^{2KM\times(N_d+2)}$. This can now be expressed as

$$\overline{\boldsymbol{A}}_{\boldsymbol{f}}(\bar{\boldsymbol{s}}_0) = \begin{bmatrix} \tilde{\boldsymbol{U}}^{\top} & c \times \mathbf{1}_{KM\times 1} & \mathbf{0}_{KM\times 1} \\ \tilde{\boldsymbol{U}}^{\top} & c \times \mathbf{1}_{KM\times 1} & \bar{\boldsymbol{\lambda}}^{\top} \end{bmatrix}, \tag{35}$$

where $\bar{\boldsymbol{\lambda}} = [\lambda_1, \cdots, \lambda_K]^{\top} \otimes \mathbf{1}_{1\times \mathrm{M}} \in \mathbb{R}^{1\times \mathrm{KM}}$. The differential integer ambiguity is $\bar{\boldsymbol{z}}_{\mathrm{d}} = \overline{\boldsymbol{D}}\boldsymbol{z}$, where the differentiator matrix $\overline{\boldsymbol{D}}$ has the form $\overline{\boldsymbol{D}} = \left[-\mathbf{1}_{(KM-1)\times 1}\ \boldsymbol{I}_{(KM-1)}\right] \in \mathbb{R}^{(KM-1)\times KM}$, and the matrix $\overline{\boldsymbol{E}} = \left[\mathbf{0}_{(KM-1)\times 1}, \boldsymbol{I}_{KM-1}\right]^{\top} \in \mathbb{R}^{KM\times(KM-1)}$.

The remaining steps proceed as described in the second stage. To extend the algorithm to the nonuniform assignment case, or to completely disjoint bands, which represent a specific case of nonuniform assignment, we can select any existing integer ambiguity as the reference to define φ_{d} and construct $\bar{\boldsymbol{z}}_{\mathrm{d}}$. The matrices $\overline{\boldsymbol{D}}$ and $\overline{\boldsymbol{E}}$ are then trivially updated accordingly. Additionally, for $\overline{\boldsymbol{A}}_{\boldsymbol{s}_0}$ and $\boldsymbol{B}$, we remove the rows and columns corresponding to measurements that no longer exist.

VI. Numerical Results and Insights

We next investigate and evaluate the derived multi-band CPP bounds in a concrete network deployment context. Furthermore, we assess the accuracy and robustness of the proposed estimators in this setting and demonstrate the tightness of the derived bound, identifying the conditions under which the estimator attains it. More specifically, we consider an example physical scenario where the UE is located at $\boldsymbol{x}_{\mathrm{ue}} = [5.2\ \ 11.4]^{\top}\mathrm{m}$, while M BSs or other network nodes/TRPs surrounds UE with fixed locations as illustrated and shown in Fig. 4. This is the default network deployment assumed in majority of the results while also the sensitivity against the locations of the network nodes is assessed, as part of the results collection. Each location has been obtained as a realization of a $\mathcal{N}(\boldsymbol{x}_{\mathrm{ue}}, (0.1\,\mathrm{km})^2\boldsymbol{I}_{2\times 2})$ random variable. Furthermore, the following default system parameters are utilized, unless otherwise stated: subcarrier spacing $\Delta_{f,k} = 30\,\mathrm{kHz}$, $N_k = 612$ subcarriers (51 NR resource blocks, per band), noise power spectral density of $-174\,\mathrm{dBm/Hz}$, a receiver noise figure of $13\,\mathrm{dB}$, and $M = 6$ BSs. We model the magnitude of the channel gain as $\rho_{m,k} = \lambda_{\mathrm{ref}}/(4\pi\|\boldsymbol{x}_{\mathrm{bs},m} - \boldsymbol{x}_{\mathrm{ue}}\|)$ with $\lambda_{\mathrm{ref}} = 3\,\mathrm{cm}$. Therefore, we assume that transceiver array gain essentially compensates the dependence of the path loss factor with respect to a reference frequency of $10\,\mathrm{GHz}$. The default per-band transmit power is $P_{\mathrm{tx},k} = 0\,\mathrm{dBm}$. As the default carrier frequencies at different bands, we use $f_c = 3.5\,\mathrm{GHz}$

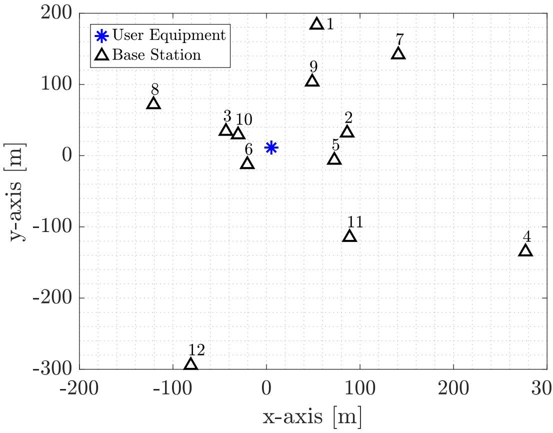

Fig. 4. 2D map of default BS locations and the UE. The numbers next to the BSs indicate their selection order when varying the number of BSs. In the default setup with six BSs, nodes BS_1 to BS_6 are considered.

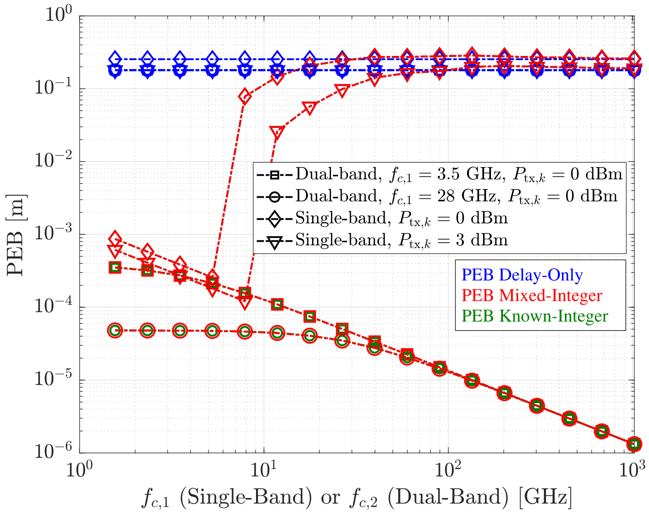

Fig. 5. Impact of the carrier frequency on the different PEBs. For the single-band case, a doubled P_{tx} case is also shown for fair comparison.

(FR1), $f_c = 28\,\mathrm{GHz}$ (FR2), and $f_c = 12\,\mathrm{GHz}$ (FR3), unless otherwise stated. The number of iterations for the second stage of Algorithm 1 is set to $N_{\mathrm{iter}} = 2$, the default number of search points is set to $N_s = 1$ and the confidence interval used by the deterministic sampling method is set to $T_\alpha = 4$.

For assessing and comparing the impacts of the different parameters, we use the PEB defined as $\mathrm{PEB} = \sqrt{\mathrm{tr}(\boldsymbol{\Sigma}_\star(\boldsymbol{x}_{\mathrm{ue}}))}$ for all the mixed-integer, known-integer, and delay-only bounds, while the evaluation metric for the estimator is the root-mean-square error (RMSE), expressed as

$$\mathrm{RMSE} = \sqrt{\frac{\sum_{i=1}^{N_{mc}} \|\hat{\boldsymbol{x}}_{\mathrm{ue},i} - \boldsymbol{x}_{\mathrm{ue}}\|^2}{N_{mc}}}. \tag{36}$$

The proposed MICRB given in (21) and the RMSE are computed over $N_{\mathrm{mc}} = 1\,000$ Monte-Carlo samples.

A. Carrier Frequency and Multi-Band Measurements

We start by illustrating the impact of carrier frequency while also comparing the single-band and dual-band scenarios.

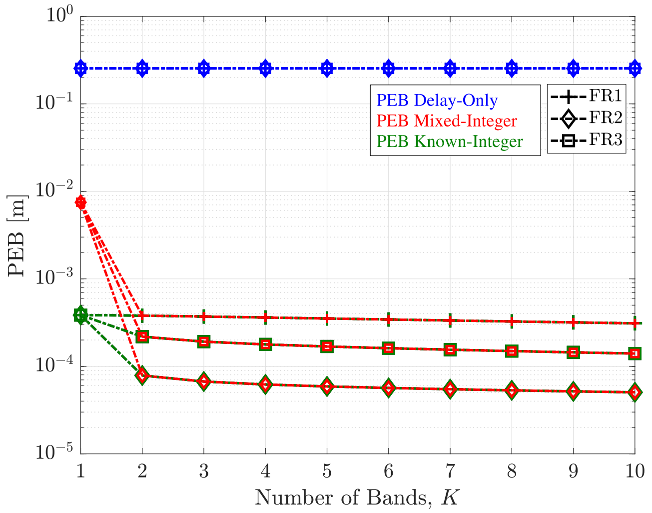

Fig. 6. PEB vs. the number of measurement frequencies, K. In all cases, the first carrier frequency ($f_{c,1}$) correspond to 3.5 GHz, while the additional frequencies follow the frequency ranges indicated in the text.

The results are shown in Fig. 5. In the single-band case, $f_{c,1}$ varies, whereas in the dual-band case $f_{c,1}$ is fixed and $f_{c,2}$ varies. The delay-only PEB ($\mathrm{PEB}_{\mathrm{delay}}$) appears unaffected by the carrier frequency, as it primarily depends on SNR and bandwidth rather than the frequency (assuming a constant SNR across bands). In contrast, the known-integer PEB ($\mathrm{PEB}_{\mathrm{known}}$)–plotted only for the dual-band case for the readability of figure–improves with increasing carrier frequency since shorter wavelengths reduce the power of the measurement noise in (5). In mathematical terms, $\mathrm{PEB}_{\mathrm{known}}$ is governed by $\boldsymbol{\Sigma}_\vartheta$, which improves as λ decreases. For higher values of $f_{c,2}$, the influence of $f_{c,1}$ disappears, and both dual-band cases coincide.

Furthermore, the behavior of the proposed mixed-integer PEBs ($\mathrm{PEB}_{\mathrm{mi}}$) reveals more interesting insights. In the single-band case, the $\mathrm{PEB}_{\mathrm{mi}}$ curves converge to $\mathrm{PEB}_{\mathrm{known}}$ for carrier frequencies below $f_{c,1} = 9\,\mathrm{GHz}$ (with doubled TX power) and $f_{c,1} = 5\,\mathrm{GHz}$ (default TX power). This means that the reduced-state ambiguities are fully resolved below these frequency thresholds. At higher frequencies, however, the curves diverge since shorter wavelengths lower the probability of correct ambiguity resolution. In other words, the integer program (17) becomes harder to solve correctly at higher frequencies. In the dual-band case, unlike single-band scenario, no divergence is observed, and $\mathrm{PEB}_{\mathrm{mi}}$ coincides with $\mathrm{PEB}_{\mathrm{known}}$ across all $f_{c,2}$ values. This improved performance stems from the diversity provided by measurements whose ambiguities are multiples of different wavelengths,which enables more reliable ambiguity resolution. Even when $f_{c,1} = 28\,\mathrm{GHz}$ and $f_{c,2} > 100\,\mathrm{GHz}$, we still have $\mathrm{PEB}_{\mathrm{mi}} = \mathrm{PEB}_{\mathrm{known}}$, whereas in the single-band cases, the convergence does not occur for either $f_{c,1} = 28\,\mathrm{GHz}$ or $f_{c,1} \geq 100\,\mathrm{GHz}$.

Next, Fig. 6 illustrates the combined effect of carrier frequency and the number of measurement bands, K. To fairly assess the impact of the number of bands, we maintain constant sum-power of $K \times P_{\mathrm{tx},k} = 0\,\mathrm{dBm}$ for any given K. For $K = 1$, all curves correspond to $f_{c,1} =$

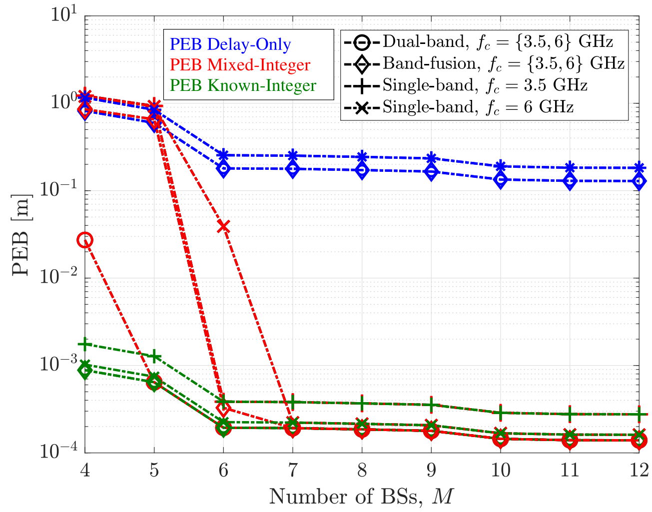

Fig. 7. Comparison between the multi-band and single-band fusion approaches while also varying the number of base stations, M.

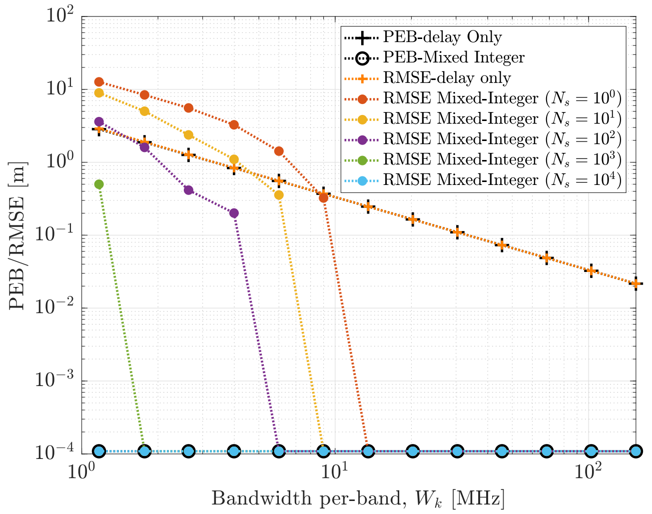

Fig. 8. The random-search refinement results for different bandwidths in a dual-band FR1&FR3 case. The x-axis shows the bandwidth for each band.

3.5 GHz, while when K increases from 2 to 10, we include sequentially the following carrier frequencies in the different bands: FR1: $[3.6{:}0.2{:}5.2]$ GHz, FR2: $[24{:}1{:}32]$ GHz, and FR3: $[8{:}0.5{:}12]$ GHz. Thus overall, FR1 adopts intra-band CA, while the other cases correspond to inter-band CA. As shown in Fig. 6, $\mathrm{PEB}_{\mathrm{delay}}$ remains constant as the number of bands K increases. This is because the benefit of additional measurements is balanced by the reduced transmit power per band, and the new measurements do not provide a different type of information; only the noise realizations differ across bands. In contrast, $\mathrm{PEB}_{\mathrm{mi}}$ and $\mathrm{PEB}_{\mathrm{known}}$ improve for two reasons. First, having more bands introduces additional measurements that contain new information about the location, as the integer ambiguities differ across bands. This effect is especially noticeable when increasing from a single-band to dual-band. Second, the higher carrier frequencies of the added bands tighten the bound, as previously discussed in Fig. 5. For $K \geq 2$, $\mathrm{PEB}_{\mathrm{mi}}$ is completely coincided with $\mathrm{PEB}_{\mathrm{known}}$.

B. Comparison of the Proposed Multi-Band Bound With Existing Single-Band Bounds

To verify the optimality of the proposed multi-band mixed-integer bound, we provide a comparison between the single-band bounds proposed in [9], their fusion across bands, and the multi-band bounds in our work. To obtain the fusion of separate single-band cases, we sum up the effective FIM matrices[7] of the position and clock bias parameters (i.e., the inverse of the upper-left $(N_d+1)\times(N_d+1)$ block of the full CRB matrix) of each band and compute the corresponding covariance matrices. This approach is followed because each band has distinct phase offsets as unknown parameters, so we focus on the effective FIM for the common parameters across all bands.

As shown in Fig. 7, the $\mathrm{PEB}_{\mathrm{known}}$ and $\mathrm{PEB}_{\mathrm{delay}}$ bounds are identical in both the multi-band and the band-fusion cases, since different bands provide linear measurements with independent noise and real-valued phase offsets which are solved independently for each band. Therefore, the multi-band FIM is equal to the sum of the individual FIMs. However, the behavior differs for $\mathrm{PEB}_{\mathrm{mi}}$. In this case, the multi-band $\mathrm{PEB}_{\mathrm{mi}}$ formulation implicitly assumes that all integer ambiguities are resolved jointly, while the band-fusion $\mathrm{PEB}_{\mathrm{mi}}$ formulation assumes they are solved independently within each band. The observed improvement in the multi-band $\mathrm{PEB}_{\mathrm{mi}}$ therefore reflects the benefits of jointly estimating interrelated integer parameters (an effect absent in $\mathrm{PEB}_{\mathrm{known}}$ and $\mathrm{PEB}_{\mathrm{delay}}$, which involve only real parameters). As a result, the joint resolution of two interrelated sets of integer ambiguities provides more reliable ambiguity estimation and yields faster convergence in the multi-band $\mathrm{PEB}_{\mathrm{mi}}$ compared to the band-fusion case.

The effect of the number of BSs, M, is also assessed and highlighted in Fig. 7. While increasing M generally improves performance, the improvement is not strictly linear due to the involved randomness in BS placement (additional BSs are dropped randomly in the area, cf. Fig. 4). Importantly, the multi-band mixed-integer PEB reaches convergence with fewer BSs than the other cases.

C. Performance Evaluation of the Proposed Estimator

1) Search-Based Optimization: To evaluate the performance of Algorithm 1, we examine its RMSE under different bandwidths and varying numbers of candidate points (N_s), which are used as initial solutions after the algorithm's first stage. In the following, the candidate points are generated using random sampling as explained in Section IV-C, whereas the deterministic sampling method is considered separately in Section VI-C6. The corresponding $\mathrm{PEB}_{\mathrm{delay}}$ and $\mathrm{PEB}_{\mathrm{mi}}$ bounds are used as benchmarks. Fig. 8 presents the results for a dual-band scenario involving FR1 and FR3 aggregation.

As shown, the RMSE curves of the algorithm's first stage (delay-only) converge to the $\mathrm{PEB}_{\mathrm{delay}}$ for all bandwidths. However, in the case of $N_s = 1$, which corresponds to a

---

[7] The effective part of the FIM matrix is obtained by computing the Schur complement of the FIM block associated with the phase offset.

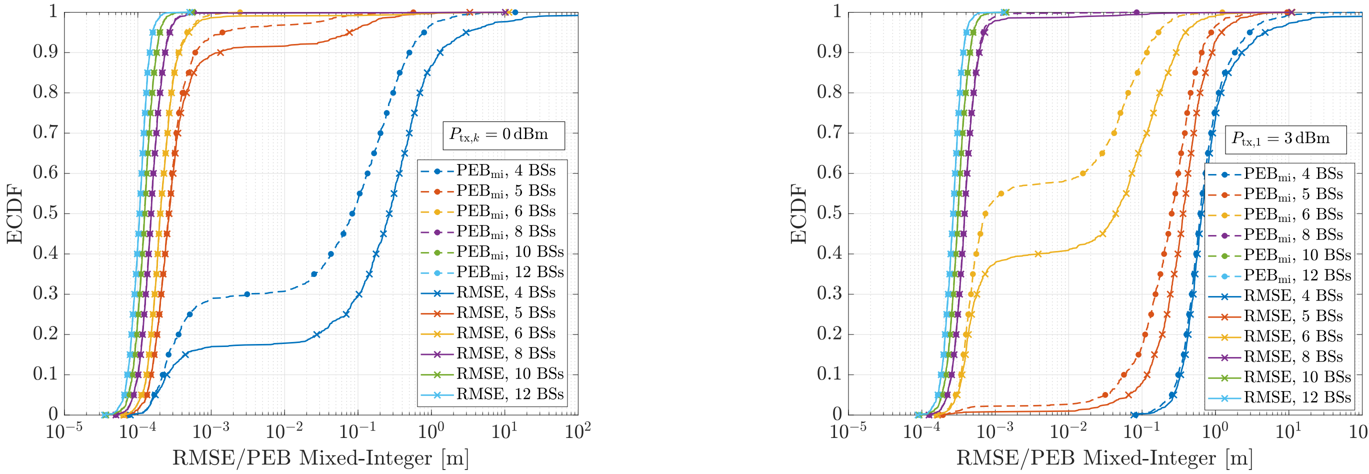

(a) Dual-band case with $f_c = \{3.5,\ 12\}$ GHz.

(b) Single-band case with $f_c = 3.5\,\text{GHz}$.

Fig. 9. CDFs of the RMSE and the mixed-integer PEB for different numbers of BSs, evaluated over 1 000 independent random BS geometries.

scenario without a search process, the narrowband regime (less than 13.5 MHz) reveals that even the $\text{PEB}_{\text{delay}}$ accuracy is insufficient for full convergence in the second stage. Moreover, within this bandwidth range, large integer errors in several Monte-Carlo trials cause the final RMSE to exceed that of the delay-only stage. Nevertheless, the case of $N_s = 1$ remains practical for CPP in a wide range of applications, as the bandwidths available in 5G NR and future 6G networks typically exceed 13.5 MHz. As the number of search points increases to $N_s = 1\,000$, the convergence point of the algorithm improves from $W = 13.5\,\text{MHz}$ to $W = 2.65\,\text{MHz}$, making it more suitable for IoT applications. For $N_s = 10^4$, full convergence is achieved across the entire bandwidth range, albeit at the cost of higher complexity. Increasing the number of random points raises their density within a fixed region and also expands the overall area they may occupy. These factors together make it more likely that some samples fall into the attraction region of the final optimal solution, thereby ensuring convergence to the multi-band MICRB.

2) Network Geometry Effects: To assess the proposed MICRB and the estimator performance for different network geometries, we extend our analysis by considering 1 000 independent BS–UE geometries, where the BS locations are randomly drawn as $\boldsymbol{x}_{\text{bs},m} \sim \mathcal{N}(\boldsymbol{x}_{\text{ue}}, (0.1\,\text{km})^2\boldsymbol{I}_{2\times 2})$ while the user is fixed at its default location. For each geometry realization, we compute both the PEB_{mi} and the RMSE of the final CPP estimate over 1 000 Monte Carlo noise realizations. For the estimation, a random-search optimization method with up to 500 evaluation points is employed. For a fair comparison, the per-band transmit power is doubled in the single-band case. For each randomly selected geometry, we also change the number of BSs progressively.

Now, as can be observed in the CDF curves in Fig. 9a, in the dual-band case, when more than five BSs are available, the RMSE curves closely follow the mixed-integer PEB curves, and nearly all geometries achieve sub-millimeter accuracy. Even in the five-BS case, approximately 90% of the geometries attain sub-millimeter accuracy, with RMSE performance tightly matching the corresponding bounds. In contrast, for the single-band scenario shown in Fig. 9b, geometry-induced degradation is clearly observed: For six BSs and fewer, degenerate geometries lead to a significant performance loss. With six BSs, more than 40% of the geometries fail to achieve sub-centimeter accuracy, even when an efficient estimator is employed. These results indicate that the multi-band configuration exhibits substantially improved robustness to geometric impairments, enabling reliable high-accuracy positioning with fewer anchor nodes.

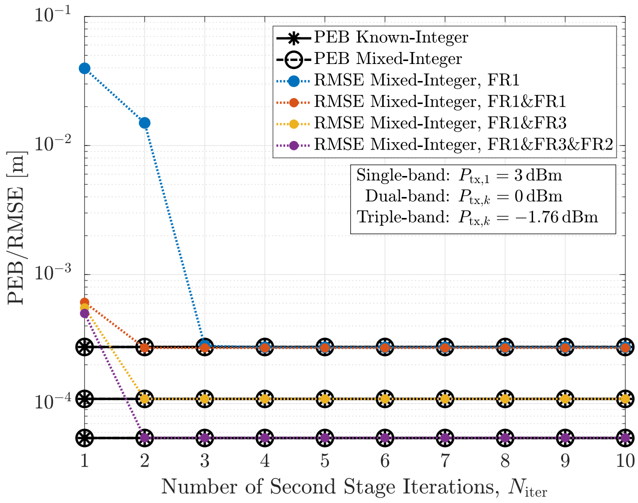

Fig. 10. Impact of the number of second stage iterations on estimator performance. Single-band FR1 corresponds to $f_c = 3.5\,\text{GHz}$, FR1&FR1 to $f_c = \{3.5, 3.6\}$ GHz, FR1&FR3 to $f_c = \{3.5, 12\}$ GHz, and the triple-band FR1&FR3&FR2 case to $f_c = \{3.5, 12, 28.1\}$ GHz.

3) Number of Second Stage Iterations: We next study the impact of the number of iterations, N_{iter}, by evaluating the RMSE as N_{iter} increases in an example scenario with a minimal bandwidth of 13.7 MHz (456 subcarriers). As shown in Fig. 10, all cases except the single-band FR1 converge to their corresponding MICRB already by the second iteration. Nevertheless, the iterative algorithm also appears promising

TABLE I
CONSIDERED BS-BAND ASSIGNMENT PATTERNS

Assignment	Type of allocation	BS1	BS2	BS3	BS4	BS5	BS6
6b–1BS/b	6-band disjoint	3.5	7.5	11.5	15.5	19.5	23.5
6b–2BS/b	6-band nonuniform	3.5, 7.5	3.5, 7.5	11.5, 15.5	11.5, 15.5	19.5, 23.5	19.5, 23.5
3b–2BS/b	triple-band nonuniform	3.5	3.5	7.5	7.5	11.5	11.5
3b–6BS/b	triple-band uniform	3.5, 7.5, 11.5	3.5, 7.5, 11.5	3.5, 7.5, 11.5	3.5, 7.5, 11.5	3.5, 7.5, 11.5	3.5, 7.5, 11.5
1b–6BS/b	single-band uniform	3.5	3.5	3.5	3.5	3.5	3.5

6b–1BS/b means 6 bands with 1 BS per band; 6b–2BS/b means 6 bands with 2 BSs per band, etc. All frequencies are in GHz.

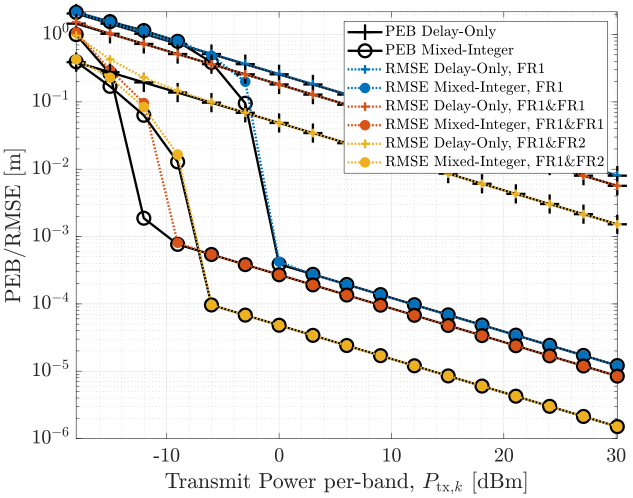

Fig. 11. RMSE versus transmit power in different CA cases. Single-band FR1 corresponds to $f_c = 3.5\,$GHz, FR1&FR1 to $f_c = \{3.5, 3.6\}$ GHz, and FR1&FR2 to $f_c = \{3.5, 28\}$ GHz.

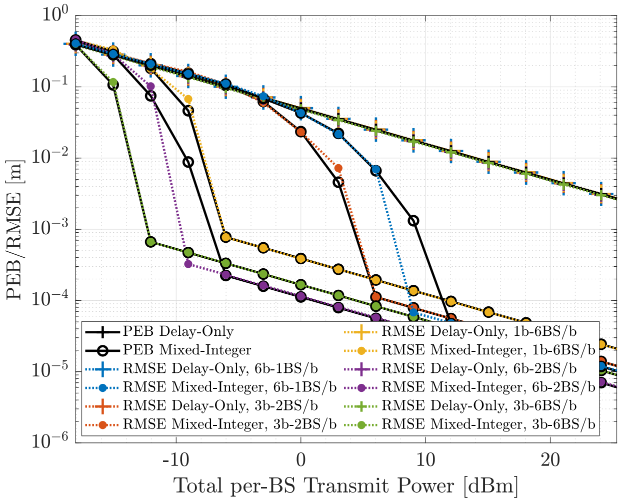

Fig. 12. RMSE versus total per-BS transmit power for nonuniform BS-Band assignment. All the curves corresponds to the band-independent phase offset scenarios, while the details of the assignments are as shown in Table I.

for the single-band case, as convergence starts from the third iteration. To ensure fairness, the total transmit power per BS is kept identical across all scenarios. In the following results, we thus set $N_{\text{iter}} = 2$, while noting that a more general stopping criterion could also be developed and applied.

4) Power Budget Analysis: We next consider default practical bandwidths for each frequency range, i.e., $20\,$MHz for FR1 and $100\,$MHz for FR2. Under these settings, the accuracy of the proposed estimator closely aligns with the MICRB across different per-band transmit power levels. Note that the carrier phase and delay error variances are related to the TX power via (7)–(9). As shown in Fig. 11, the first RMSE curve corresponds to single-band FR1 transmission. While it follows the MICRB, compared to the dual-band cases, its convergence to the asymptotic RMSE occurs more slowly (starting from $0\,$dBm), and also the asymptotic RMSE is higher. In dual-band configurations, the estimator reaches lower asymptotic RMSE values more quickly. Specifically, FR1&FR1 achieves faster convergence (starting from $-9\,$dBm), whereas FR1&FR2, results in a lower asymptotic RMSE, at the cost of a slightly slower convergence rate (starting from $-6\,$dBm), due to the higher carrier frequency of FR2.

5) Nonuniform BS-Band Assignment: We now consider an observation model where the phase offset φ_{ue} is band-independent. Five different BS-band assignment patterns are analyzed and considered, illustrated in Table I, to demonstrate that the proposed bounds remain valid under such situations too, and that the estimators converge to the bounds successfully. First, we examine an extreme case where each BS is assigned to a distinct band in the range $f_c = 3.5{:}4{:}23.5\,$GHz, referred to as the 6b–1BS/b pattern. Note that this scenario is feasible if and only if the phase offset is band-independent. We also consider the 6b-2BS/b pattern for the same set of bands, where each band is assigned to two BSs; since there are $M = 6$ BSs, each BS operates in a dual-band mode. Next, we evaluate a 3b-2BS/b pattern, where three bands with $f_c = 3.5{:}4{:}11.5\,$GHz are each shared by two BSs (each BS operating within a single band). We also consider the fully uniform 3b-6BS/b assignment pattern of this triple-band case, where each BS operates in the same three bands. A fully uniform assignment case of a single-band scenario (denoted as 1b-6BS/b), in which all BSs operate on the same band at $f_c = 3.5\,$GHz is also considered. The bandwidth of each band is around $100\,$MHz (3168 subcarriers). To ensure a fair comparison, the x-axis represents the total per-BS transmit power (rather than per-band transmit power $P_{\mathrm{tx},k}$), so that all BS-band assignments are evaluated under the same total power budget.

As shown in Fig. 12, the delay-only RMSE is identical for all patterns, stemming essentially from the constant sum-power. The 6b-2BS/b configuration outperforms 6b-1BS/b, 3b-2BS/b, and 1b-6BS/b, highlighting the benefit of multi-band operation. In other words, 6b-1BS/b and 3b-2BS/b correspond to nonuniform single-band cases, while 6b-2BS/b

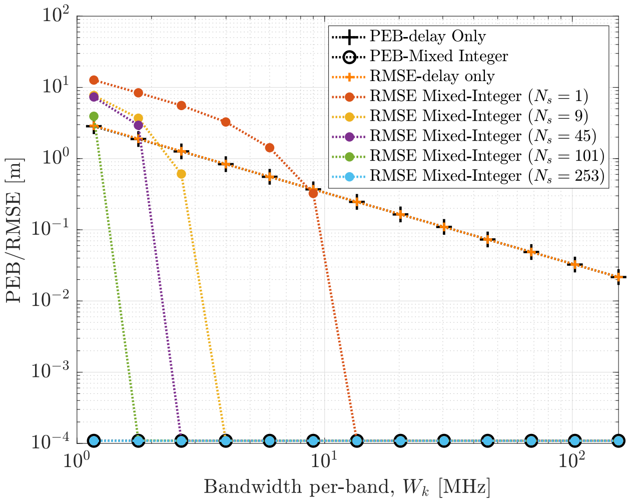

Fig. 13. RMSE results for the proposed deterministic-search refinement approach for different bandwidths in a dual-band FR1&FR3 case. The x-axis shows the bandwidth for each band.

represents a nonuniform dual-band case. The 6b-2BS/b pattern also achieves a lower converged RMSE than the fully uniform 3b-6BS/b case because some BSs operate at higher carrier frequencies in 6b-2BS/b. However, the 3b-6BS/b configuration converges faster than 6b-2BS/b, mainly due to its lower average carrier frequency and the fact that it involves triple-band operation.

Finally, comparing 1b-6BS/b, 3b-2BS/b, and 6b-1BS/b assignments, we can observe that the uniform case 1b-6BS/b converges faster than the other ones, again due to its lower carrier frequency. The same reasoning explains the faster convergence of 3b-2BS/b compared to 6b-1BS/b. It should be noted that the multi-band advantage is not observed in the 3b-2BS/b and 6b-1BS/b configurations, since multi-band benefits arise only when an individual BS has access to multi-band measurements, allowing for the interrelated ambiguities of the same BS to be resolved jointly.[8]

6) Improved Performance-Complexity Tradeoffs via Deterministic Sampling: Next, we evaluate the performance of the proposed deterministic sampling scheme presented in Section IV-C under varying number of deterministic candidate points and different bandwidths. The RMSE curves for a dual-band scenario involving FR1 and FR3 aggregation are shown in Fig. 13 and the results are benchmarked with respect to $\text{PEB}_{\text{delay}}$ and PEB_{mi}. The results clearly indicate that the deterministic sampling scheme has superior performance-complexity tradeoffs when compared to the random sampling counterpart for which the results are illustrated in Fig. 8. As an example, the deterministic search only requires nine candidate points to achieve the PEB_{mi} at $W = 4.0\,\text{MHz}$, whereas the random sampling method requires $N_s > 100$. Furthermore, full convergence is achieved across the entire bandwidth range with deterministic sampling using $N_s = 253$ candidate points which is a notable reduction in computational complexity with respect to the random sampling scheme that requires $N_s = 10\,000$ for full convergence. It is to be noted that removing candidate points with very low probability is important to obtain a computationally efficient algorithm. The deterministic sampling method that achieves full convergence utilizes a 51st order Hermite polynomial resulting in 2601 candidate points. However, only $9.73\,\%$ of these candidate points are within the $T_\alpha = 4$ confidence interval (see Fig. 3), meaning that $2\,348$ candidate points are located in areas with extremely low probability. Following the Gaussian assumption of the initial delay-only estimate, the squared error is expected to follow a chi-squared distribution meaning that only 0.03% of the times the ground truth location is outside the $T_\alpha = 4$ confidence interval. Therefore, if we only consider evaluation points that satisfy $\|\boldsymbol{\xi}^{(n)}\| \leq T_\alpha$, we do not expect any significant performance degradation and the number of candidate points can be reduced significantly. The deterministic sampling method was also tested without candidate point removal ($T_\alpha = \infty$), and the results were nearly identical to those illustrated in Fig. 13.

D. Estimator Sensitivity Analysis

Finally, we analyze the sensitivity of the proposed estimator to imperfections caused by network-side clock uncertainties and multi-path propagation, while comparing the dual-band and single-band configurations. To ensure a fair comparison, the total transmit power is again kept identical in both cases.

1) Sensitivity to Network Clock Imperfections: We model clock bias imperfections as normally distributed random offsets [15], common across all bands but independent across BSs. To account for this in both the bound derivation and the estimator design, the error covariance matrices $\boldsymbol{\Sigma}_\tau, \boldsymbol{\Sigma}_\vartheta$, and $\boldsymbol{\Sigma}_{\text{ch}}$ are updated according to subsection III-D. In Fig. 14a, we assess and show the estimator and bound performance for different values of standard deviation (STD) of the clock uncertainty, δ_m, which is assumed to be identical across all BSs. As an additional benchmark, we also consider a configuration aided by a reference receiver, referred to as a positioning reference unit (PRU), with a known location at $\boldsymbol{x}_{\text{pru}} = [0 \quad 0]^\top$, which enables CPP performance invariant to network-side synchronization imperfections. The related formulations regarding PRU-based measurements are provided in Appendix C.

As depicted, CPP results are considerably more sensitive to clock imperfections than TDoA-based localization since the clock jitter affects both delay and phase measurements. Since the variance of phase errors is much smaller than that of delay errors, the impact on CPP performance becomes more pronounced. However, compared to the single-band case, the multi-band mechanism improves the robustness of CPP against clock uncertainties, under an equal total transmit power constraint. Notably, the robustness gain of the multi-band case appears only in the PEB_{mi} and mixed-integer RMSE curves, while the delay-only and known-integer curves closely match those of the single-band case. This observation indicates that the robustness gain of multi-band CPP against imperfect synchronization primarily originates from its enhanced integer ambiguity resolution capability. In the considered scenario,

---

[8] Ambiguities of different BSs are already related through the geometry, and assigning each BS to a different band does not introduce additional interrelations.

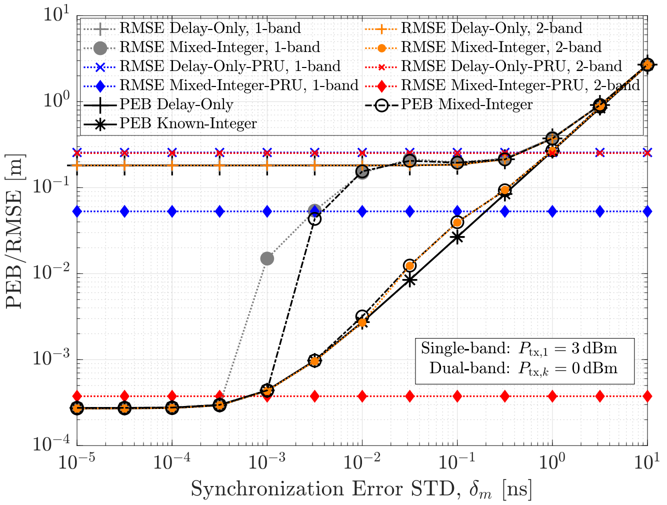

(a) Network clock uncertainties

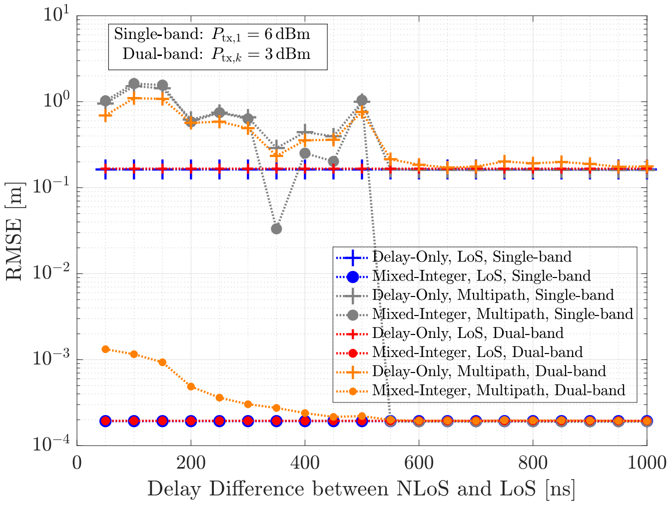

(b) Multipath delay difference

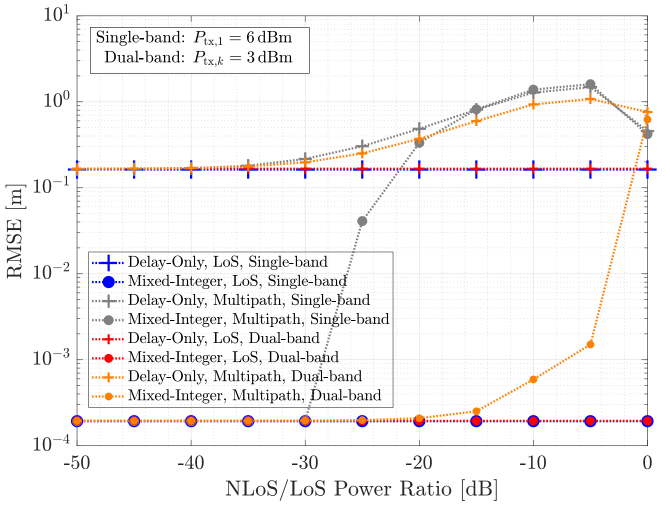

(c) Multipath power ratio

Fig. 14. RMSE performance versus different imperfections. Single-band case corresponds to $f_c = 3.5\,\text{GHz}$, and the dual-band case uses $f_c = \{3.5, 3.6\}\,\text{GHz}$. For fair comparison, the single-band case is evaluated with doubled P_{tx}.

when the synchronization error STD is less than 100 picoseconds, the multi-band CPP method remains robust and achieves an acceptable RMSE performance whereas the single-band configuration requires synchronization accuracy better than 3 ps to maintain comparable robustness.

We should note that achieving synchronization accuracy on the order of 100 ps remains challenging in realistic network deployments. However, such tight synchronization constitutes a fundamental requirement of CPP-based positioning and is likewise essential for emerging distributed network architectures, including cell-free and distributed massive MIMO systems. Consequently, sub-nanosecond to picosecond-level synchronization has been studied and achieved theoretically in the contexts of CPP-based inter-BS synchronization [15] and distributed massive MIMO systems [48], and has also been developed and demonstrated experimentally within wired networks through CERN's White Rabbit project [49], indicating active efforts toward fulfilling this requirement in both academia and industry.

A more practical approach for mitigating network-side synchronization imperfections is to employ PRUs. The results in Fig. 14a confirm that the PRU-based approach effectively eliminates sensitivity to clock uncertainties. Since the differential measurement noises are stronger than UE measurement noises, the PRU-based results exhibit higher RMSE compared to ordinary CPP under perfect synchronization.

2) Sensitivity to Multi-Path Propagation: We consider a dual-path scenario consisting of a LoS and one non-line-of-sight (NLoS) component. As in the previous cases, the measurements are restricted to a single OFDM symbol. The dominant paths, along with their corresponding delay and carrier phase measurements, are detected and estimated using the Hankel-based ESPRIT algorithm described in [50] and [51]. The path with the lowest delay is then selected as the LoS, and positioning is performed based on the estimated parameters of this path. We analyze the performance of the dual-band and single-band CPP under different delay differences between the LoS and NLoS paths as well as different NLoS-to-LoS power ratios. The LoS-only scenarios are included as benchmarks.

In Fig. 14b, the sensitivity of the proposed estimator to NLoS interference is illustrated as a function of the delay difference between the LoS and NLoS paths. The NLoS-to-LoS power ratio is $-6\,\text{dB}$ in this example. As the delay difference increases, the two paths become more distinguishable, and in both the single-band and dual-band cases, the mixed-integer RMSE of the multi-path scenario converges to that of the LoS case. In contrast, for small delay separations, the reduced accuracy of the delay estimation results in increased phase estimation errors, which consequently degrade the final CPP accuracy. A key observation is the superior robustness of the dual-band estimator across the entire range of delay differences. In particular, for delay differences below 500 ns, the single-band case shows limited robustness, while the dual-band case maintains stable performance. Although for very short delays (less than 200 ns) the dual-band mixed-integer RMSE exceeds the LoS benchmark, it still outperforms the delay-only estimator and achieves an accuracy around 1 millimeter.

In Fig. 14c, the delay difference between the NLoS and LoS paths is fixed at 100 ns (corresponding to 30 m), while

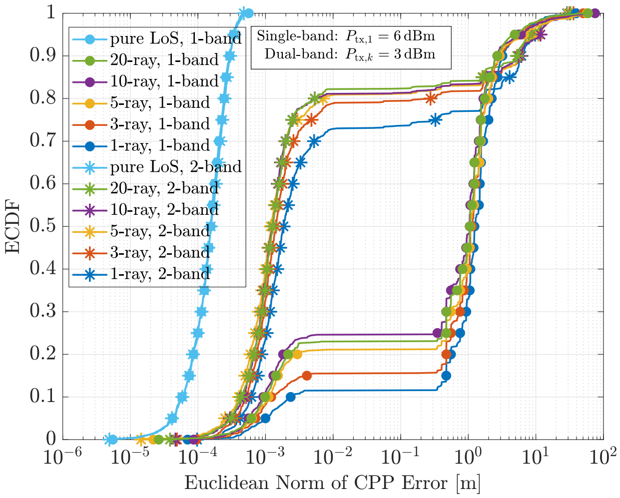

Fig. 15. CDFs of the CPP position errors for different numbers of NLoS rays. The single-band case uses $f_c = 3.5\,\mathrm{GHz}$, while the dual-band case operates at $f_c = \{3.5,\ 3.6\}\,\mathrm{GHz}$. The delay separation between the first NLoS ray and the LoS path is $30\,\mathrm{ns}$.

the NLoS-to-LoS power ratio is varied. The curves show that the single-band CPP estimator exhibits poor robustness and fails to outperform the delay-only benchmark for NLoS/LoS power ratios greater than $-20\,\mathrm{dB}$. In contrast, the dual-band estimator consistently outperforms the delay-only RMSE of the pure LoS scenario up to NLoS/LoS power ratio of $-5\,\mathrm{dB}$. For higher NLoS/LoS power ratios, the NLoS component acts as strong interference. Since the path delays are close to each other, resolving the LoS and NLoS paths becomes increasingly difficult.

Finally, to examine more complex multi-path scenarios involving clustered NLoS propagation, we model the channel using the Saleh–Valenzuela model [52], where the arrivals of NLoS rays follow a Poisson process. We consider a scenario with a total NLoS/LoS power ratio of $-6\,\mathrm{dB}$ and a $30\,\mathrm{ns}$ delay separation between the first NLoS ray and the LoS path. Fig. 15 shows the CDFs of the positioning errors for the CPP estimator in both single-band and dual-band configurations. For both cases, the pure LoS performance is very similar; however, compared to the single-band case, the dual-band configuration exhibits increased robustness to clustered multi-path impairments. Given that the CDF curves corresponding to different numbers of rays are closely grouped, the results indicate that that positioning performance is primarily governed by the separation between the LoS and NLoS components, while the detailed structure of the NLoS paths (e.g., clustering) plays a less significant role. As the figure illustrates, for a fixed total NLoS-to-LoS power ratio, increasing the number of rays spreads the NLoS power across weaker components, which facilitates more accurate LoS separation.

VII. CONCLUSION

This work addressed multi-band cellular carrier phase positioning, integrating both intra-band and inter-band carrier aggregation to enhance positioning accuracy. We introduced and derived the fundamental mixed-integer Cramér-Rao bound, specifically tailored for multi-band positioning. As critical performance benchmarks, we also derived the lower bounds for delay-only and known-integer ambiguity cases. We then proposed a practical two-stage CPP estimator. By incorporating a search-based optimization in the second stage, we demonstrated that the estimator remains efficient even in low-bandwidth regimes. The offered results highlight the advantages of multi-band positioning measurements, demonstrating their ability to improve localization accuracy over single-band approaches–particularly, in terms of resolving integer ambiguities and thereby reducing positioning errors. Additionally, we showed the impact of different carrier frequencies, carrier bandwidths, and the number of base stations, offering valuable design insights for next-generation positioning systems. Notably, we showed that aggregating just two carriers can already significantly improve integer ambiguity resolution while also offering improved robustness against system imperfections imposed by degenerate network geometry, network-side clock uncertainties and multi-path propagation. Finally, we extended the bound derivations and CPP estimator study to scenarios where different base-stations may use partially or totally disjoint frequencies. Future work will focus on developing reduced-complexity yet efficient CPP estimators, including sampling strategies that adapt to the quality of the initial position estimate, as well as virtual-frequency-aided CPP that facilitate integer ambiguity resolution in multi-band systems. Extensions of the CPP framework to dynamic scenarios and tracking of moving UEs will also be investigated.

APPENDIX A
MULTI-BAND RELAXED INTEGER AMBIGUITY BOUND

We consider $\boldsymbol{z}_{\mathrm{rlx}}$ as a real-valued parameter vector in the observation model (14). Accordingly, the unknown parameter vector is defined as $\boldsymbol{\eta} = [\tilde{\boldsymbol{s}}^{\top}, {\boldsymbol{z}_{\mathrm{rlx}}}^{\top}]^{\top} \in \mathbb{R}^{(KM+N_d+1)\times 1}$, and the corresponding FIM matrix can be expressed as

$$\boldsymbol{J}_{\mathrm{rlx}}(\boldsymbol{\eta}) = \begin{bmatrix} \tilde{\boldsymbol{U}}\boldsymbol{J}\tilde{\boldsymbol{U}}^{\top} & c\tilde{\boldsymbol{U}}\mathrm{diag}(\boldsymbol{J}) & \tilde{\boldsymbol{U}}\boldsymbol{J}_{\vartheta}\boldsymbol{\Lambda}^{\top} \\ c(\tilde{\boldsymbol{U}}\mathrm{diag}(\boldsymbol{J}))^{\top} & \mathrm{tr}(\boldsymbol{J})c^2 & c(\boldsymbol{\Lambda}\mathrm{diag}(\boldsymbol{J}_{\vartheta}))^{\top} \\ \boldsymbol{\Lambda}(\tilde{\boldsymbol{U}}\boldsymbol{J}_{\vartheta})^{\top} & c\boldsymbol{\Lambda}\mathrm{diag}(\boldsymbol{J}_{\vartheta}) & \boldsymbol{\Lambda}\boldsymbol{J}_{\vartheta}\boldsymbol{\Lambda}^{\top} \end{bmatrix} \tag{37}$$

where $\boldsymbol{J} = \boldsymbol{J}_{\vartheta} + \boldsymbol{J}_{\tau}$, and $\boldsymbol{J}_{\vartheta} = \boldsymbol{\Sigma}_{\vartheta}^{-1}$. Note that $\boldsymbol{\Lambda}$, $\tilde{\boldsymbol{U}}$, and $\boldsymbol{J}_{\tau}$ are already defined in (10), (22). By applying the well-known Schur complement to the FIM, it can be shown that the lower bound for the error covariance of $\boldsymbol{z}_{\mathrm{rlx}} \in \mathbb{R}^{KM\times 1}$ is then of the form

$$\boldsymbol{\Sigma}_{\mathrm{rlx}} = \boldsymbol{\Lambda}^{-1}\boldsymbol{\Sigma}_{\vartheta}\boldsymbol{\Lambda}^{-1} + \boldsymbol{\Lambda}^{-1}\begin{bmatrix} \tilde{\boldsymbol{U}}^{\top} & c\mathbf{1}_{KM\times 1} \end{bmatrix} \boldsymbol{J}_{\mathrm{delay}}^{-1}(\tilde{\boldsymbol{s}}) \begin{bmatrix} \tilde{\boldsymbol{U}} \\ c\mathbf{1}_{1\times KM} \end{bmatrix} \boldsymbol{\Lambda}^{-1}. \tag{38}$$

Furthermore, for the observation model (14), it can be shown that the error covariance bound on $\tilde{\boldsymbol{s}}$ is the same as the delay-only case in (22).

APPENDIX B
MULTI-BAND KNOWN INTEGER AMBIGUITY BOUND

When $\boldsymbol{z}_{\mathrm{d}}$ is known in the observation model (12), the FIM of $\boldsymbol{s}$ is given by

$$\boldsymbol{J}_{\text{known}}(\boldsymbol{s}) = \begin{bmatrix} \tilde{\boldsymbol{U}}\boldsymbol{J}\tilde{\boldsymbol{U}}^\top & c\tilde{\boldsymbol{U}}\mathrm{diag}(\boldsymbol{J}) & \tilde{\boldsymbol{U}}\boldsymbol{J}_\vartheta\tilde{\boldsymbol{\Lambda}}^\top \\ c(\tilde{\boldsymbol{U}}\mathrm{diag}(\boldsymbol{J}))^\top & \mathrm{tr}(\boldsymbol{J})c^2 & c(\tilde{\boldsymbol{\Lambda}}\mathrm{diag}(\boldsymbol{J}_\vartheta))^\top \\ \tilde{\boldsymbol{\Lambda}}(\tilde{\boldsymbol{U}}\boldsymbol{J}_\vartheta)^\top & c\tilde{\boldsymbol{\Lambda}}\mathrm{diag}(\boldsymbol{J}_\vartheta) & \tilde{\boldsymbol{\Lambda}}\boldsymbol{J}_\vartheta\tilde{\boldsymbol{\Lambda}}^\top \end{bmatrix} \tag{39}$$

where $\tilde{\boldsymbol{\Lambda}} = \mathrm{diag}([\lambda_1, \cdots, \lambda_K]^\top) \otimes \mathbf{1}_{1\times M} \in \mathbb{R}^{K\times KM}$. Taking the inverse of $\boldsymbol{J}_{\text{known}}(\boldsymbol{s})$, the error covariance bound on the position reads as $\boldsymbol{\Sigma}_{\text{known}}(\boldsymbol{x}_{\mathrm{ue}}) = [\boldsymbol{J}_{\text{known}}(\boldsymbol{s})]^{-1}_{1:N_d,1:N_d}$.

APPENDIX C
MULTI-BAND PRU-BASED MEASUREMENT MODEL

Since the position of the reference receiver is known, we can formulate the PRU delay and phase measurements associated with the m-th BS and k-th band as follows

$$y_{\mathrm{pru},\tau,m,k} = B_{\mathrm{pru}}c + \tilde{B}_m c + \omega_{\mathrm{pru},\tau,m,k} \tag{40}$$

$$\begin{aligned} y_{\mathrm{pru},\vartheta,m,k} &= z_{\mathrm{pru},m,k}\lambda_k + \varphi_{\mathrm{pru},k}\lambda_k \\ &\quad + B_{\mathrm{pru}}c + \tilde{B}_m c + \omega_{\mathrm{pru},\vartheta,m,k} \end{aligned} \tag{41}$$

where the known BS-PRU range term is removed from both sides of the equations. The notation is consistent with previous definitions, with the subscript $\star_{\mathrm{pru}}$ used to distinguish PRU-related variables. The measurement noises follow the same statistical model as those at the UE, with the variances depending on the BS–PRU distance, denoted by $\sigma^2_{\mathrm{pru},\tau,m,k}$ and $\sigma^2_{\mathrm{pru},\vartheta,m,k}$ for delay and phase measurements, respectively. By differencing the measurements in (40) and (41) from the UE measurements in (23) and (24), we obtain the differential measurements of the form

$$y_{\mathrm{dd},\tau,m,k} = \|\boldsymbol{x}_{\mathrm{bs},m} - \boldsymbol{x}_{\mathrm{ue}}\| + B_{\mathrm{dd}}c + \omega_{\mathrm{dd},\tau,m,k} \tag{42}$$

$$\begin{aligned} y_{\mathrm{dd},\vartheta,m,k} &= \|\boldsymbol{x}_{\mathrm{bs},m} - \boldsymbol{x}_{\mathrm{ue}}\| + z_{\mathrm{dd},m,k}\lambda_k + \varphi_{\mathrm{dd},k}\lambda_k \\ &\quad + B_{\mathrm{dd}}c + \omega_{\mathrm{dd},\vartheta,m,k} \end{aligned} \tag{43}$$

where $\star_{\mathrm{dd}} = \star_{\mathrm{ue}} - \star_{\mathrm{pru}}$ for all variables and the differential noise variance is $\sigma^2_{\mathrm{dd},\star,m,k} = \sigma^2_{\mathrm{pru},\star,m,k} + \sigma^2_{\star,m,k}$. The resulting differential measurements are invariant to network-side synchronization imperfections and have the same functional form as (4) and (5). Therefore, the proposed CPP estimation algorithm and bound derivations can be directly applied also to the differential measurements.

REFERENCES

[1] *Study on Expanded and Improved NR Positioning (Release 18)*, document TR 38.859, 3GPP, Jun. 2024.

[2] J. Nikonowicz, A. Mahmood, M. I. Ashraf, E. Björnson, and M. Gidlund, "Indoor positioning in 5G-advanced: Challenges and solution toward centimeter-level accuracy with carrier phase enhancements," *IEEE Wireless Commun.*, vol. 31, no. 4, pp. 268–275, Aug. 2024.

[3] P. J. G. Teunissen and A. Khodabandeh, "Review and principles of PPP-RTK methods," *J. Geodesy*, vol. 89, no. 3, pp. 217–240, Mar. 2015.

[4] N. González-Prelcic et al., "The integrated sensing and communication revolution for 6G: Vision, techniques, and applications," *Proc. IEEE*, vol. 112, no. 7, pp. 676–723, Jul. 2024.

[5] X. Li and K. Pahlavan, "Super-resolution TOA estimation with diversity for indoor geolocation," *IEEE Trans. Wireless Commun.*, vol. 3, no. 1, pp. 224–234, Jan. 2004.

[6] S. Gezici et al., "Localization via ultra-wideband radios: A look at positioning aspects for future sensor networks," *IEEE Signal Process. Mag.*, vol. 22, no. 4, pp. 70–84, Jul. 2005.

[7] P. Axelrad, C. J. Comp, and P. F. Macdoran, "SNR-based multipath error correction for GPS differential phase," *IEEE Trans. Aerosp. Electron. Syst.*, vol. 32, no. 2, pp. 650–660, Apr. 1996.

[8] J. Mo, Z. Deng, B. Jia, H. Jiang, and X. Bian, "A novel FLL-assisted PLL with fuzzy control for TC-OFDM carrier signal tracking," *IEEE Access*, vol. 6, pp. 52447–52459, 2018.

[9] H. Wymeersch, R. Amiri, and G. Seco-Granados, "Fundamental performance bounds for carrier phase positioning in cellular networks," in *Proc. IEEE Global Commun. Conf. (GLOBECOM)*, Dec. 2023, pp. 7478–7483.

[10] J. Talvitie, M. Säily, and M. Valkama, "Orientation and location tracking of XR devices: 5G carrier phase-based methods," *IEEE J. Sel. Topics Signal Process.*, vol. 17, no. 5, pp. 919–934, Sep. 2023.

[11] X. Zhang, T. Wang, Z. Yao, and M. Lu, "Centimeter-level carrier phase positioning for ground-based positioning system without synchronization," *IEEE Trans. Veh. Technol.*, vol. 73, no. 10, pp. 15345–15358, Oct. 2024.

[12] K. Berntorp, A. Weiss, and S. D. Cairano, "Integer ambiguity resolution by mixture Kalman filter for improved GNSS precision," *IEEE Trans. Aerosp. Electron. Syst.*, vol. 56, no. 4, pp. 3170–3181, Aug. 2020.

[13] F. Ayten et al., "Phase-only positioning: Overcoming integer ambiguity challenge through deep learning," in *Proc. IEEE 36th Int. Symp. Pers., Indoor Mobile Radio Commun. (PIMRC)*, Sep. 2025, pp. 1–7.

[14] Y. Wu, M. F. Keskin, U. Gustavsson, G. Seco-Granados, E. G. Larsson, and H. Wymeersch, "Location and map-assisted wideband phase and time calibration between distributed antennas," 2024, *arXiv:2410.23120*.

[15] S. Fan, W. Ni, H. Tian, Z. Huang, and R. Zeng, "Carrier phase-based synchronization and high-accuracy positioning in 5G new radio cellular networks," *IEEE Trans. Commun.*, vol. 70, no. 1, pp. 564–577, Jan. 2022.

[16] A. Fouda, R. Keating, and H.-S. Cha, "Toward cm-level accuracy: Carrier phase positioning for IIoT in 5G-advanced NR networks," in *Proc. IEEE 33rd Annu. Int. Symp. Pers., Indoor Mobile Radio Commun. (PIMRC)*, Sep. 2022, pp. 782–787.

[17] L. Chen, X. Zhou, F. Chen, L.-L. Yang, and R. Chen, "Carrier phase ranging for indoor positioning with 5G NR signals," *IEEE Internet Things J.*, vol. 9, no. 13, pp. 10908–10919, Jul. 2022.

[18] Z. Peng, S. Fan, and H. Tian, "Carrier phase-based localization method for TDD systems via extended Kalman filter," in *Proc. IEEE Wireless Commun. Netw. Conf. (WCNC)*, Apr. 2024, pp. 1–6.

[19] X. Han et al., "Flexible spectrum orchestration of carrier aggregation for 5G-advanced," *IEEE Commun. Standards Mag.*, vol. 7, no. 4, pp. 68–74, Dec. 2023.

[20] C.-X. Wang et al., "On the road to 6G: Visions, requirements, key technologies, and testbeds," *IEEE Commun. Surveys Tuts.*, vol. 25, no. 2, pp. 905–974, 2nd Quart., 2023.

[21] M. Säily, O. N. C. Yilmaz, D. S. Michalopoulos, E. Pérez, R. Keating, and J. Schaepperle, "Positioning technology trends and solutions toward 6G," in *Proc. IEEE 32nd Annu. Int. Symp. Pers., Indoor Mobile Radio Commun. (PIMRC)*, Sep. 2021, pp. 1–7.

[22] W. Xu, S. Shojaee, and K. Manolakis, "Carrier-aggregated timing estimation for radio positioning," in *Proc. IEEE 89th Veh. Technol. Conf. (VTC-Spring)*, Apr. 2019, pp. 1–7.

[23] T. Kazaz, G. J. M. Janssen, J. Romme, and A.-J. van der Veen, "Delay estimation for ranging and localization using multiband channel state information," *IEEE Trans. Wireless Commun.*, vol. 21, no. 4, pp. 2591–2607, Apr. 2022.

[24] Z. Wei et al., "Carrier aggregation enabled integrated sensing and communication signal design and processing," *IEEE Trans. Veh. Technol.*, vol. 73, no. 3, pp. 3580–3596, Mar. 2024.

[25] M. Cocard, S. Bourgon, O. Kamali, and P. Collins, "A systematic investigation of optimal carrier-phase combinations for modernized triple-frequency GPS," *J. Geodesy*, vol. 82, no. 9, pp. 555–564, Sep. 2008.

[26] Y. Feng, "GNSS three carrier ambiguity resolution using ionosphere-reduced virtual signals," *J. Geodesy*, vol. 82, no. 12, pp. 847–862, Dec. 2008.

[27] J. Li et al., "Optimal carrier phase combinations for triple-frequency GNSS derived from an analytical method," *Acta geodaetica et cartographica sinica*, vol. 41, no. 6, pp. 797–803, May 2012.

[28] Q. Zhao, Z. Dai, Z. Hu, B. Sun, C. Shi, and J. Liu, "Three-carrier ambiguity resolution using the modified TCAR method," *GPS Solutions*, vol. 19, no. 4, pp. 589–599, Oct. 2015.

[29] A. Saikko, J. Talvitie, and M. Valkama, "High-precision 3D location and orientation tracking using multi-sensor cellular carrier phase measurements," in *Proc. 33rd Eur. Signal Process. Conf. (EUSIPCO)*, Sep. 2025, pp. 915–919.

[30] J. Li, M. Liu, S. Shang, X. Gao, and J. Liu, "Carrier phase positioning using 5G NR signals based on OFDM system," in *Proc. IEEE 96th Veh. Technol. Conf. (VTC-Fall)*, Sep. 2022, pp. 1–5.

[31] S. Fan, Y. Ji, and H. Tian, "Triple-frequency carrier phase positioning with optimized ambiguity resolution in 5G new radio networks," in *Proc. Global Commun. Conf. (GLOBECOM)*, Dec. 2023, pp. 1191–1196.

[32] E. Shourezari et al., "Multi-band carrier phase positioning toward 6G: Performance bounds and design insights," in *Proc. IEEE ICC*, May 2026, pp. 1–7.

[33] H. Wymeersch and G. Seco-Granados, "Radio localization and sensing—Part I: Fundamentals," *IEEE Commun. Lett.*, vol. 26, no. 12, pp. 2816–2820, Dec. 2022.

[34] J. S. Subirana, J. M. J. Zornoza, and M. Hernández-Pajares, "ESA TM-23 GNSS data processing," European Space Agency, Noordwijk, The Netherlands, Tech. Rep. TM-23, 2013.

[35] S. M. Kay, *Fundamentals of Statistical Signal Processing: Estimation Theory*. Upper Saddle River, NJ, USA: Prentice-Hall, 1993.

[36] Y. C. Eldar, "Uniformly improving the CramÉr–Rao bound and maximum-likelihood estimation," *IEEE Trans. Signal Process.*, vol. 54, no. 8, pp. 2943–2956, Aug. 2006.

[37] J. Ou, S. Fan, and H. Tian, "Single-shot carrier phase positioning method with wrapping effect solution in 5G new radio cellular networks," in *Proc. IEEE Global Commun. Conf. (GLOBECOM)*, Dec. 2024, pp. 313–318.

[38] R. Amiri, F. Behnia, and A. Noroozi, "An efficient estimator for TDOA-based source localization with minimum number of sensors," *IEEE Commun. Lett.*, vol. 22, no. 12, pp. 2499–2502, Dec. 2018.

[39] Y. T. Chan and K. C. Ho, "A simple and efficient estimator for hyperbolic location," *IEEE Trans. Signal Process.*, vol. 42, no. 8, pp. 1905–1915, Aug. 1994.

[40] J. Smith and J. Abel, "Closed-form least-squares source location estimation from range-difference measurements," *IEEE Trans. Acoust., Speech, Signal Process.*, vol. ASSP-35, no. 12, pp. 1661–1669, Dec. 1987.

[41] K. C. Ho and Y. T. Chan, "Solution and performance analysis of geolocation by TDOA," *IEEE Trans. Aerosp. Electron. Syst.*, vol. 29, no. 4, pp. 1311–1322, Oct. 1993.

[42] G. Mellen, M. Pachter, and J. Raquet, "Closed-form solution for determining emitter location using time difference of arrival measurements," *IEEE Trans. Aerosp. Electron. Syst.*, vol. 39, no. 3, pp. 1056–1058, Jul. 2003.

[43] P. J. Teunissen, "Least-squares estimation of the integer GPS ambiguities," in *Proc. Sect. 4th Theory Methodol., IAG Gen. Meeting*, Beijing, China, 1993, pp. 1–16.

[44] S. Särkkä and L. Svensson, *Bayesian Filtering and Smoothing*, 2nd ed., Cambridge, U.K.: Cambridge Univ. Press, 2023.

[45] X.-W. Chang, X. Yang, and T. Zhou, "MLAMBDA: A modified LAMBDA method for integer least-squares estimation," *J. Geodesy*, vol. 79, no. 9, pp. 552–565, Dec. 2005.

[46] P. S. Farahsari, A. Farahzadi, J. Rezazadeh, and A. Bagheri, "A survey on indoor positioning systems for IoT-based applications," *IEEE Internet Things J.*, vol. 9, no. 10, pp. 7680–7699, May 2022.

[47] *Discussion of NR Positioning Enhancements*, document R1-2003642, 3GPP, Jun. 2020.

[48] U. Kunnath Ganesan, R. Sarvendranath, and E. G. Larsson, "BeamSync: Over-the-air synchronization for distributed massive MIMO systems," *IEEE Trans. Wireless Commun.*, vol. 23, no. 7, pp. 6824–6837, Jul. 2024.

[49] P. Moreira, P. Alvarez, J. Serrano, I. Darwezeh, and T. Wlostowski, "Digital dual mixer time difference for sub-nanosecond time synchronization in Ethernet," in *Proc. IEEE Int. Freq. Control Symp.*, Jun. 2010, pp. 449–453.

[50] H. Dun, C. C. J. M. Tiberius, and G. J. M. Janssen, "Positioning in a multipath channel using OFDM signals with carrier phase tracking," *IEEE Access*, vol. 8, pp. 13011–13028, 2020.

[51] B. Yang, K. B. Letaief, R. S. Cheng, and Z. Cao, "Channel estimation for OFDM transmission in multipath fading channels based on parametric channel modeling," *IEEE Trans. Commun.*, vol. 49, no. 3, pp. 467–479, Mar. 2001.

[52] A. A. M. Saleh and R. Valenzuela, "A statistical model for indoor multipath propagation," *IEEE J. Sel. Areas Commun.*, vol. JSAC-5, no. 2, pp. 128–137, Feb. 1987.